

Detection of relic gravitational waves in the CMB: Prospects for CMBPol mission

Wen Zhao^{1,2,3,*}

¹*International Center for Astrophysics, Korea Astronomy and Space Science Institute, Daejeon, 305-348, Korea*

²*School of Physics and Astronomy, Cardiff University, Cardiff, CF24 3AA, United Kingdom*

³*Department of Physics, Zhejiang University of Technology, Hangzhou, 310014, P.R.China*

(Dated: October 15, 2018)

Abstract

Detection of relic gravitational waves, through their imprint in the cosmic microwave background radiation, is one of the most important tasks for the planned CMBPol mission. In the simplest viable theoretical models the gravitational wave background is characterized by two parameters, the tensor-to-scalar ratio r and the tensor spectral index n_t . In this paper, we analyze the potential joint constraints on these two parameters, r and n_t , using the potential observations of the CMBPol mission, which is expected to detect the relic gravitational waves if $r \gtrsim 0.001$. The influence of the contaminations, including cosmic weak lensing, various foreground emissions, and systematical errors, is discussed.

PACS numbers: 98.70.Vc, 98.80.Cq, 04.30.-w

arXiv:1102.4908v1 [astro-ph.CO] 24 Feb 2011

*Electronic address: wzha07@kasi.re.kr

I. INTRODUCTION

The detection of primordial gravitational waves is rightly considered a highest priority task for the upcoming observation missions [1]. A stochastic background of the relic gravitational waves (RGWs), produced in the very early Universe due to the superadiabatic amplification of zero point quantum fluctuations of the gravitational field, is a necessity dictated by general relativity and quantum mechanics [2]. So the detection of RGWs may provide the unique way to study the birth of the Universe, and test the applicability of general relativity and quantum mechanics in the very high energy scale [3].

In a whole range of scenarios of the early Universe, the primordial power spectrum of the RGWs can be well described by a power-law form in a fairly large frequency range [4–9]. Thus, the RGW backgrounds are conventionally simply characterized by two parameters, the so-called tensor-to-scalar ratio r and the primordial power spectral index of RGWs n_t , where r describes the amplitude of the primordial spectrum, and n_t denotes the tilt of the spectrum. So the constraints on r and n_t will give us a direct glimpse into the physical conditions in the early Universe. In particular, they will allow us to place the constraints on the Hubble parameter of the early Universe, and time evolution of this Hubble parameter. Unfortunately, the models of the early Universe cannot give a definite prediction for the values of r and n_t , i.e., different inflationary models predict the quite different values of r and n_t [10], especially some string motivated inflationary models predict a very small gravitational waves with $r \ll 10^{-4}$ [11]. So, the only way to determine them is by the observations.

The RGWs leave well understood imprints on the anisotropies in temperature and polarization of cosmic microwave background radiation (CMB) [12–18]. More specifically, RGWs produce a specific pattern of polarization in the CMB known as the B -mode polarization [13]. Moreover, RGWs produce a negative cross-correlation between the temperature and polarization known as the TE -correlation at the low multipoles $\ell \lesssim 50$ [17, 18]. The theoretical analysis of these imprints along with the data from CMB experiments allows to place constraints on the parameters r and n_t describing the RGW background, which provides the unique way to detect the RGWs at the very low frequencies ($10^{-17} \sim 10^{-15}$ Hz).

The current CMB experiments are yet to detect a definite signature of RGWs [19], although a hint of RGWs is found in the WMAP data [20]. A number of authors have discussed the possibility of RGW detection by the launched Planck satellite [20–23]. The results show that, due to the fairly large instrumental noises, only if the tensor-to-scalar ratio is large ($r \gtrsim 0.05$), the Planck satellite is expected to have a detection. In the previous paper [24], we also found that the Planck mission cannot give a good constraint for the spectral index n_t , even if the tensor-to-scalar ratio is as large as $r = 1$. In addition, various ground-based [25] and balloon-borne [26] CMB experiments are expected to have the better detection abilities, which can constrain the parameter r fairly well when $r \gtrsim 0.01$. However, an accurate constraint of n_t is still unexpected, due to the small partial sky observation or the short time observation [27].

The accurate determination of the RGWs requires the full sky and the long time observations by the CMB experiment with the quite small instrumental noises. The future space-based mission focus on the CMB polarization [28] (here and in the following, we use the label ‘CMBPol’ to refer it) provides an excellent opportunity to realize it (the similar projects, such as B-Pol [29] and LiteBird [30], are also proposed). The instrumental noises of CMBPol mission are more than 100 times smaller than those of Planck mission. If the foreground contaminations and the systematical errors can be well controlled, the signature of RGWs can be well detected, as long as $r \gtrsim 0.001$ [28]. This will provide an observational tool to distinguish the different inflationary-type models.

In this paper we shall analyze the joint constraints on two parameters r and n_t that would be feasible with the analysis of the observations from the planned CMBPol mission. We shall detailedly discuss the constraints of r , n_t and the best-pivot wavenumber k_t^* depending on the input (or true) value of the tensor-to-scalar ratio r . We discuss the effects of various contaminations from the cosmic weak lensing, foreground radiations and the beam systematics.

The outline of the paper is as follows. In Sec. II we shall introduce and explain the notations for the power spectra of gravitational waves, density perturbations and various CMB anisotropy fields. Furthermore, in this section, we shall briefly introduce the existence of the best-pivot wavenumber k_t^* for the detection of RGWs in the CMB. The analytical formulae and explanation for the k_t^* , Δr and Δn_t will also be discussed. In Sec. III, by using the analytical formulae and only considering the instrumental noises, we shall discuss the values of k_t^* , Δr and Δn_t for different input (or true) value of r . Sec. IV is contributed to show the effect of the cosmic lensing contamination, and Sec. V is contributed to show the effect of the foreground radiations contamination. In Sec. VI, we discuss the effects of various beam systematics for the determination of the parameters r and n_t . We also discuss the requirement of the CMBPol’s systematics, if the biases of the parameters r and n_t are ignorable. Finally, Sec. VII is dedicated to a brief discussion and conclusion.

II. OPTIMAL PARAMETERS AND THEIR DETERMINATIONS

The main contribution to the observed temperature and polarization anisotropies of the CMB comes from two types of the cosmological perturbations, density perturbations (also known as the scalar perturbations) and RGWs (also known as the tensor perturbations) [6, 7, 12, 13], which are generally characterized by their primordial power spectra. These power spectra are usually assumed to be power-law, which is a generic prediction of a wide range of scenarios of the early Universe, including the inflationary models. In general there might be deviations from a power-law, which can be parameterized in terms of the running of the spectral index (see for example [10, 31]), but we shall not consider this possibility in the current paper. Thus, the power spectra of the perturbation fields have the form

$$P_s(k) = A_s(k_0)(k/k_0)^{n_s-1}, \quad P_t(k) = A_t(k_0)(k/k_0)^{n_t}, \quad (1)$$

for density perturbations and RGWs respectively. In the above expression k_0 is an arbitrarily chosen pivot wavenumber, n_s is the primordial power spectral index for density perturbations, and n_t is the primordial power spectral index for RGWs. $A_s(k_0)$ and $A_t(k_0)$ are normalization coefficients determining the absolute values of the primordial power spectra at the pivot wavenumber k_0 . The choices of $n_s = 1$ and $n_t = 0$ correspond to the scale-invariant power spectra for density perturbations and gravitational waves respectively.

The relative contribution of density perturbations and gravitational waves is described by the so-called tensor-to-scalar ratio r , which is defined as follows

$$r(k_0) \equiv \frac{A_t(k_0)}{A_s(k_0)}. \quad (2)$$

Note that, in defining the tensor-to-scalar ratio r , we have not used any inflationary formulae which relate r with the physical conditions during inflation and the slow-roll parameters (see for example [32]). Thus, our definition depends only on the power spectral amplitudes of density perturbations and RGWs, and does not assume a particular generating mechanism for these cosmological perturbations. The RGW amplitude $A_t(k_0) = r(k_0)A_s(k_0)$ provides us with direct information on the Hubble parameter of the very early Universe [31]. More specifically, this amplitude is directly related to the value of the Hubble parameter H at a time when wavelengths corresponding to the wavenumber k_0 crossed the horizon [33]

$$A_t^{1/2}(k_0) = \frac{\sqrt{2}}{M_{\text{pl}}} \frac{H}{\pi} \Big|_{k_0/a=H}, \quad (3)$$

where $M_{\text{pl}} = 1/\sqrt{8\pi G}$ is the reduced Planck mass. If we adopt $A_s = 2.445 \times 10^{-9}$ as predicted by the WMAP5 observations [34], the Hubble parameter is $H \simeq 2.67r^{1/2} \times 10^{14} \text{ GeV}$, only depending on the value of r . In the canonical single-field slow-roll inflationary models, the Hubble parameter directly relates to the energy scale of inflation $V^{1/4}$. The relation (3) follows that $V^{1/4} \simeq 3.35r^{1/4} \times 10^{16} \text{ GeV}$, which has been emphasized by a number of authors.

Assuming that the amplitude of density perturbations $A_s(k_0)$ is known, taking into account the definitions (1) and (2), the power spectrum of the RGW field may be completely characterized by tensor-to-scalar ratio r and the spectral index n_t . It is important to mention that, for spectral indices different from the scale-invariant case (i.e., when $n_s \neq 1$ or/and $n_t \neq 0$), the definition of the tensor-to-scalar ratio depends on the pivot wavenumber k_0 . If we adopt a different pivot wavenumber k_1 , the tensor-to-scalar ratio at this new pivot wavenumber $r(k_1)$ is related to original ratio $r(k_0)$ through the following relation (which follows from the definitions (1) and (2))

$$r(k_1) = r(k_0) \left(\frac{k_1}{k_0} \right)^{n_t - n_s + 1}. \quad (4)$$

Let us now turn our attention to CMB. Density perturbations and gravitational waves produce temperature and polarization anisotropies in the CMB, which are characterized by four angular power spectra C_ℓ^T , C_ℓ^C , C_ℓ^E and C_ℓ^B as functions of the multipole number ℓ . Here C_ℓ^T is the power spectrum of the temperature anisotropies, C_ℓ^E and C_ℓ^B are the power spectra of the so-called E and B modes of polarization (note that, density perturbation do not generate B -mode of polarization [13]), and C_ℓ^C is the power spectrum of the temperature-polarization cross correlation.

In general, the power spectra C_ℓ^Y (where $Y = T, E, B$ or C) can be presented in the following form

$$C_\ell^Y = C_\ell^Y(\text{dp}) + C_\ell^Y(\text{gw}), \quad (5)$$

where $C_\ell^Y(\text{dp})$ is the power spectrum due to the density perturbations, and $C_\ell^Y(\text{gw})$ is the power spectrum due to RGWs. In the case of RGWs, the CMB power spectra can be presented in the following form [14, 15]

$$\begin{aligned} C_\ell^Y(\text{gw}) &= (4\pi)^2 \int \frac{dk}{k} P_t(k) \left[\Delta_{Y\ell}^{(T)}(k) \right]^2, \quad \text{for } Y = T, E, B, \\ C_\ell^C(\text{gw}) &= (4\pi)^2 \int \frac{dk}{k} P_t(k) \left[\Delta_{T\ell}^{(T)}(k) \Delta_{E\ell}^{(T)}(k) \right]. \end{aligned} \quad (6)$$

The transfer functions $\Delta_{Y\ell}^{(T)}(k)$ (see [14, 15] for details) in the above expressions translate the power in the metric fluctuations (gravitational waves) into corresponding CMB power spectrum at an angular scale characterized by multipole ℓ . In this work, for numerical evaluation of the CMB power spectra due to density perturbations and gravitational waves, we use the publicly available CAMB code [35].

Since we are primarily interested in the parameters of the RGW field, in the analytical and numerical analysis below we shall work with a fixed cosmological background model. More specifically, we shall work in the framework of Λ CDM model, and keep the background cosmological parameters fixed at the values determined by a typical model [34]

$$h = 0.705, \quad \Omega_b h^2 = 0.02267, \quad \Omega_m h^2 = 0.1131, \quad \Omega_k = 0, \quad \tau_{\text{reion}} = 0.084, \quad A_s = 2.445 \times 10^{-9}. \quad (7)$$

Furthermore, the spectral indices of density perturbations and gravitational waves are adopted as follows for the simplicity,

$$n_s = 1, \quad n_t = 0. \quad (8)$$

Note that throughout this paper, we have considered the simplest cosmological model. In the more general consideration, one should also include the running of the spectral indices [31], the details of the reionization history [36] and so on, which have been ignored in this paper.

The CMB power spectra C_ℓ^Y are theoretical constructions determined by ensemble averages over all possible realizations of the underlying random process. However, in real CMB observations, we only have access to a single sky, and hence to a single realization. In order to obtain information on the power spectra from a single realization, it is required to construct estimators of power spectra. In order to differentiate the estimators from the actual power spectra, we shall use the notation D_ℓ^Y to denote the estimators while retaining the notation C_ℓ^Y to denote the power spectrum. It is important to keep in mind that the estimators D_ℓ^Y are constructed from observational data, while the power spectra C_ℓ^Y are theoretically predicted quantities. The probability distribution functions for the estimators are described in detail in [18] (see also [22, 37, 38]), which predicts the expectation values of the estimators

$$\langle D_\ell^Y \rangle = C_\ell^Y, \quad (9)$$

and the standard deviations

$$\begin{aligned} (\sigma_{D_\ell^X})^2 &= \frac{2(C_\ell^X + N_\ell^X)^2}{(2\ell + 1)f_{\text{sky}}}, \quad (X = T, E, B) \\ (\sigma_{D_\ell^C})^2 &= \frac{(C_\ell^T + N_\ell^T)(C_\ell^E + N_\ell^E) + (C_\ell^C + N_\ell^C)^2}{(2\ell + 1)f_{\text{sky}}}, \end{aligned} \quad (10)$$

where f_{sky} is the sky-cut factor. In this paper, we use $f_{\text{sky}} = 0.8$ for the CMBPol survey. N_ℓ^Y are the noise power spectra, which are all determined by the specific experiments. In this formulas, the possible bias generated by the beam systematics has not been considered (see Sec. VI for details).

In order to estimate the parameters r and n_t characterizing the RGW background, we shall use an analysis based on the likelihood function [39]. The likelihood function is just the probability density function of the observational data considered as a function of the unknown parameters (which are r and n_t in our case). Up to a constant, independent of its arguments, the likelihood function is given by

$$\mathcal{L} = \prod_{\ell} f(D_\ell^C, D_\ell^T, D_\ell^E, D_\ell^B),$$

where the function $f(D_\ell^C, D_\ell^T, D_\ell^E, D_\ell^B)$ is explained in detail in the previous works [22, 24].

In the previous works [22, 24], we have discussed how to constrain the parameters of the RGWs, r and n_t , by the CMB observation. In [24], we found that in general, the constraints on r and n_t correlate with each other. However,

if we consider the tensor-to-scalar ratio at the best-pivot wavenumber k_t^* , i.e. $r^* \equiv r(k_t^*)$, the constraints on r and n_t becomes independent of each other, and the uncertainties Δr and Δn_t have the minimum values. We have derived the formulae to calculate the quantities: the best-pivot wavenumber k_t^* , and the uncertainties of the parameters Δr and Δn_t , which provides a simple and quick method to investigate the detection abilities of the future CMB observations. We shall briefly introduce these results in this section.

It is convenient to define the quantities as below,

$$a_\ell^Y \equiv \frac{C_\ell^Y(\text{gw})}{\sigma_{D_\ell^Y}}, \quad b_\ell^* \equiv \ln\left(\frac{\ell}{\ell_t^*}\right), \quad d_\ell^Y \equiv \frac{D_\ell^Y - C_\ell^Y(\text{dp})}{\sigma_{D_\ell^Y}}, \quad (11)$$

where $C_\ell^Y(\text{gw})$ is the CMB power spectrum generated by RGWs, and $\sigma_{D_\ell^Y}$ is the standard deviation of the estimator D_ℓ^Y , which can be calculated by Eq. (10). We should notice that, the quantity d_ℓ^Y is dependent of random date D_ℓ^Y . By considering the relations in (9) and (5), we can obtain that $\langle d_\ell^Y \rangle = a_\ell^Y$, which shows that d_ℓ^Y is an unbiased estimator of a_ℓ^Y . ℓ_t^* is the so-called best-pivot multipole, which is determined by solving the following equation [24]:

$$\sum_\ell \sum_Y a_\ell^{Y2} b_\ell^* = 0. \quad (12)$$

So the value of ℓ_t^* depends on the cosmological model, the amplitude of RGWs, and noise power spectra by the quantity a_ℓ^Y . The best-pivot wavenumber k_t^* relates to ℓ_t^* by the approximation relation [24],

$$k_t^* \simeq \ell_t^* \times 10^{-4} \text{Mpc}^{-1}. \quad (13)$$

The numerical factor here mainly reflects the angular-diameter distance to the last scattering surface.

Once the value of ℓ_t^* is obtained, the uncertainties Δr^* and Δn_t can be calculated by the following simple formulae

$$\Delta r^* = r^* / \sqrt{\sum_\ell \sum_Y a_\ell^{Y2}}, \quad \Delta n_t = 1 / \sqrt{\sum_\ell \sum_Y (a_\ell^Y b_\ell^*)^2}. \quad (14)$$

As usual, we can define the signal-to-noise ratio $S/N \equiv r^* / \Delta r^*$. Using (14), we get

$$S/N = \sqrt{\sum_\ell \sum_Y a_\ell^{Y2}}. \quad (15)$$

In the previous work [24], we found the uncertainty of $r(k_0)$, the tensor-to-scalar ratio at the pivot wavenumber $k_0 \neq k_t^*$, is larger than Δr^* . The value of $\Delta \ln r(k_0)$ is fairly well approximated by the following formula

$$\Delta \ln r(k_0) = \sqrt{(\Delta r^* / r^*)^2 + (\ln(k_0 / k_t^*) \Delta n_t)^2}. \quad (16)$$

The smallest uncertainty on tensor-to-scalar ratio r is achieved for the choice of the pivot scale at $k_0 = k_t^*$. This justified the title ‘best’ pivot wavenumber for k_t^* . We should notice that the values of k_t^* , S/N , $\Delta \ln r$ and Δn_t only depend on the input (or true) cosmological model, but not on the data D_ℓ^Y . In Fig. 1, we plot the value of $\Delta \ln r(k_0)$ as a function of the pivot scale k_0 , where the input model has $r = 0.3$, and the Planck instrumental noises are considered (see [24] for details). As expected, when $k_0 \gg k_t^*$ or $k_0 \ll k_t^*$, the uncertainty becomes much larger than Δr^* .

The likelihood function in (11) has the maximum value at $(r_{\text{ML}}^*, n_{t\text{ML}})$. The values of r_{ML}^* and $n_{t\text{ML}}$ depend on the data D_ℓ^Y , different from the value of Δr^* and Δn_t . In the previous work [24], we found that the values of r_{ML}^* and $n_{t\text{ML}}$ can be very well approximated by the follows

$$r_{\text{ML}}^* = r^* \frac{\sum_\ell \sum_Y a_\ell^Y d_\ell^Y}{\sum_\ell \sum_Y a_\ell^{Y2}}, \quad n_{t\text{ML}} = n_t + \frac{\sum_\ell \sum_Y a_\ell^Y d_\ell^Y b_\ell^*}{\sum_\ell \sum_Y (a_\ell^Y b_\ell^*)^2}, \quad (17)$$

which depend on the data by the quantity d_ℓ^Y . If the CMB estimator D_ℓ^Y is unbiased for C_ℓ^Y , as discussed above, we have $\langle r_{\text{ML}}^* \rangle = r^*$ and $\langle n_{t\text{ML}} \rangle = n_t$, where Eq. (12) is used. These show that r_{ML}^* and $n_{t\text{ML}}$ are the unbiased estimators for r^* and n_t , respectively. However, when D_ℓ^Y is a biased estimator for C_ℓ^Y , r_{ML}^* and $n_{t\text{ML}}$ will also be the biased estimators for r^* and n_t , respectively (see Sec. VI for details), which brings the errors for the detection of RGWs.

The detection ability of the CMB experiment strongly depends on the noise levels, which include the instrumental noises, cosmic lensing contaminations, foreground radiation contaminations and the beam systematics. In the following sections, we shall discuss these effects separately. In addition, due to the partial sky survey, the leakage from the E -polarization into the B -polarization could be another kind of contamination. However, it was found that, this E - B mixture can be properly avoided (or deeply reduced) by constructing the pure E -mode and B -mode polarization fields (see [40–42] for details). So we shall not discuss this topic in this paper.

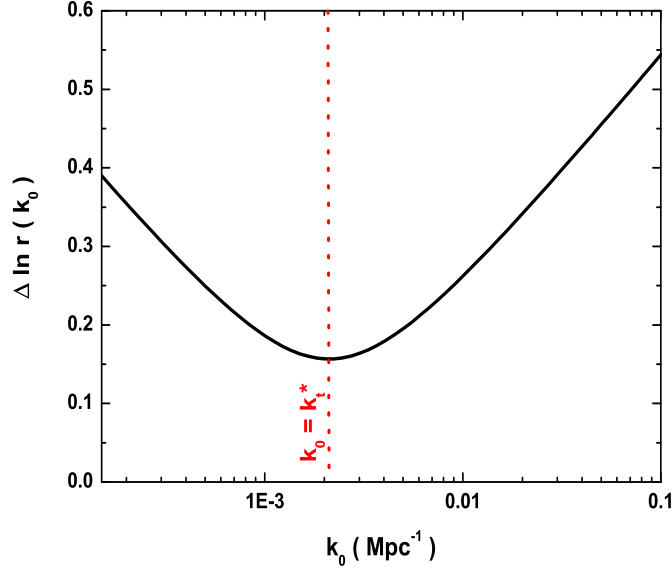


FIG. 1: The uncertainty of $r(k_0)$ for the different pivot wavenumber k_0 .

TABLE I: Experimental specifications for the mid-cost (EPIC-2m) CMBPol mission and the low-cost (EPIC-LC) CMBPol mission. [28]

EPIC-2m	Frequency [GHz]	45	70	100	150	220
	θ_F [arcmin]	17	11	8	5	3.5
	Δ_T [μ K-arcmin]	5.85	2.96	2.29	2.21	3.39
EPIC-LC	Frequency [GHz]	40	60	90	135	200
	θ_F [arcmin]	116	77	52	34	23
	Δ_T [μ K-arcmin]	15.27	8.23	3.56	3.31	3.48

III. CMBPOL INSTRUMENTAL NOISES' CONTAMINATIONS

In this section, we shall discuss the determination of RGWs, when only taking into account the instrumental noises of the CMBPol mission.

For a single frequency channel i , we assume Gaussian beams. The noise power spectrum (after deconvolution of the beam window function) is

$$N_{\text{ins},\ell}^T(i) = (\Delta_T)^2 \exp\left[\frac{\ell(\ell+1)\theta_F^2}{8 \ln 2}\right], \quad N_{\text{ins},\ell}^C(i) = 0, \quad (18)$$

and

$$N_{\text{ins},\ell}^E(i) = N_{\text{ins},\ell}^B(i) = (\Delta_P)^2 \exp\left[\frac{\ell(\ell+1)\theta_F^2}{8 \ln 2}\right], \quad (19)$$

where θ_F is the full width at half maximum (FWHM) of the beam i . Δ_T and Δ_P are the noises for the temperature and polarizations, which relate by $\Delta_P = \sqrt{2}\Delta_T$. The values of the Δ_T and Δ_P depend on the number of the detectors, the integration time and the survey area.

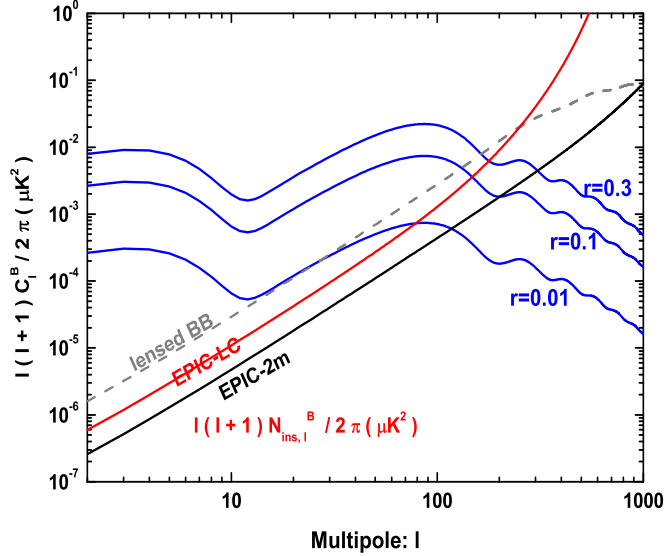


FIG. 2: The instrumental noise power spectra $N_{\text{ins},\ell}^B$ of EPIC-2m (black line) and EPIC-LC (red line).

If the experiment includes several different channels, we need to generalize the above considerations. The optimal channel combination of these channels gives the total effective instrumental noise [28],

$$[N_{\text{ins},\ell}^Y]^{-1} = \sum_i [N_{\text{ins},\ell}^Y(i)]^{-1}, \quad (20)$$

where i runs through the channels, $N_{\text{ins},\ell}^Y(i)$ is the instrumental noise bias of the channel ν_i . In this section, we shall only consider the instrumental noises, i.e.

$$N_\ell^Y \mapsto N_{\text{ins},\ell}^Y. \quad (21)$$

Since the precise experimental specifications of CMBPol have not yet been defined, we will consider two different cases (EPIC-2m) and (EPIC-LC) suggested by [28] (recently, an EPIC-Intermediate Mission is also suggested by the CMBPol team [43]). The experimental specifications are given in Table I, where 2-year design life is assumed [61]. In Fig. 2, we plot the polarization noise spectra $N_{\text{ins},\ell}^B$ of EPIC-2m and EPIC-LC, respectively [62]. For EPIC-2m, when $\ell < 100$, we find that $N_{\text{ins},\ell}^B \sim 2.7 \times 10^{-7} \mu\text{K}^2$, which is nearly 400 times smaller than that of the Planck mission (7 frequency channels from 30GHz to 353GHz and 28-month surveying time are assumed [21]). Even for the EPIC-LC, when $\ell < 100$, we have $N_{\text{ins},\ell}^B \sim 6.2 \times 10^{-7} \mu\text{K}^2$, 200 times smaller than that of the Planck mission. So comparing with Planck mission, CMBPol is much more sensitive for the detection of CMB polarization. From Fig. 2, we also find that even for the model with quite small $r = 0.01$, the value of $N_{\text{ins},\ell}^B$ is smaller than that of C_ℓ^B when $\ell < 120$ for EPIC-2m, and when $\ell < 80$ for EPIC-LC. So the CMBPol mission provides an excellent opportunity to detailedly observe the peak of C_ℓ^B at $\ell \sim 80$.

Let us discuss the constraints on the gravitational waves by the potential observations of CMBPol mission. We shall discuss the values of the best-pivot scale k_t^* , the signal-to-noise ratio S/N and the uncertainty of the spectral index Δn_t , by considering the CMBPol instrumental noises.

The value of k_t^* directly relates to the best-pivot multipole ℓ_t^* by Eq.(13), and the value of ℓ_t^* is obtained by solving the equation in (12). By using (21), we obtain the value of ℓ_t^* as a function of the input (or true) value of the tensor-to-scalar ratio r^* for EPIC-2m and EPIC-LC, which are plotted in Fig. 3 (left panel). We find that, in both cases, the value of ℓ_t^* becomes larger with the increasing of r^* . For EPIC-2m, we have $\ell_t^* = 43$ for $r^* = 0.001$, and

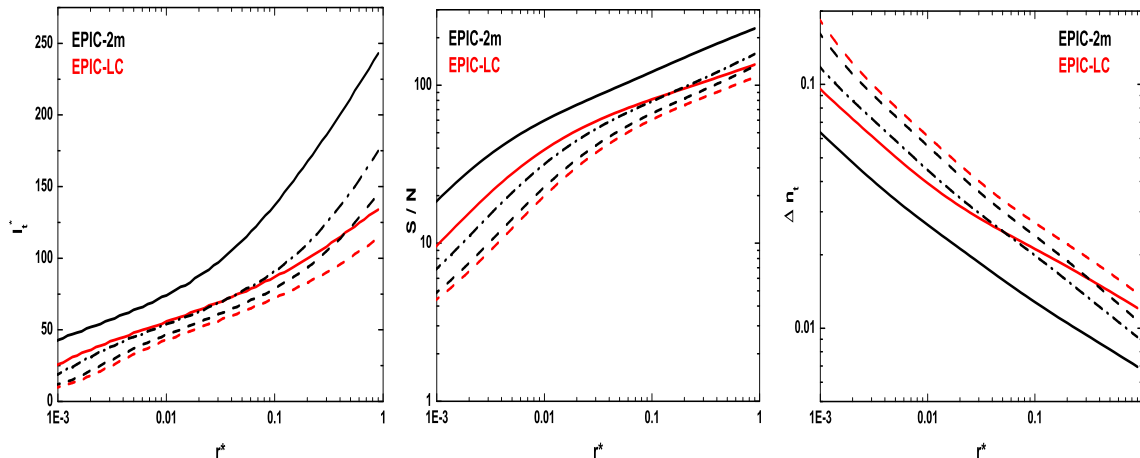


FIG. 3: The figures show the values of the best-pivot multipole ℓ_t^* (left panel), signal-to-noise ratio S/N (middle panel) and the uncertainty of the RGW spectral index Δn_t (right panel) as functions of r^* . The black solid (dash-dotted, dashed) lines correspond to the EPIC-2m instrumental noises (instrumental noises + the reduced cosmic lensing contaminations, instrumental noises + cosmic lensing contaminations), and the red solid (dashed) lines correspond to the EPIC-LC instrumental noises (instrumental noises + the cosmic lensing contaminations).

$\ell_t^* = 137$ for $r^* = 0.1$. For EPIC-LC, the value of ℓ_t^* is smaller than that of EPIC-2m, due to the larger noise level and the larger beam FWHM of EPIC-LC. When $r = 0.001$, we have $\ell_t^* = 26$, and when $r = 0.1$, we have $\ell_t^* = 87$. These reflect that gravitational waves in the frequency range $k \sim 0.01 \text{Mpc}^{-1}$ will be best constrained by the future CMBPol observations, unless the value of r is extremely small. This is because the main contribution comes from the observation of the peak of B -polarization at $\ell \sim 80$. We should remember that this is different from the Planck case, where $\ell_t^* \sim 10$, due to the main contribution of the reionization peak of B -polarization [18, 22, 24].

The signal-to-noise ratio is calculated by Eq. (15). By using Eq. (21), we get the value of S/N as a function of r^* for both EPIC-2m and EPIC-LC, which are shown in Fig. 3 (middle panel). As expected, the signal of RGWs can be very well determined by the CMBPol mission. Even for the model with $r = 0.001$, we can have $S/N = 19$ for EPIC-2m and $S/N = 10$ for EPIC-LC, when only considering the corresponding instrumental noises. When $r = 0.1$, we have $S/N = 122$ for EPIC-2m and $S/N = 81$ for EPIC-LC.

We can also calculate the value of Δn_t by using Eq. (14) and the value of ℓ_t^* given in left panel of Fig. 3. The results are shown in Fig. 3 (right panel). As expected, the value of Δn_t decreases with the increasing of r^* . For EPIC-2m, we have $\Delta n_t = 0.06$ for the model with $r^* = 0.001$, and $\Delta n_t = 0.01$ for the model with $r^* = 0.1$. This uncertainty is about 20 times smaller than that given by Planck satellite [24, 27]. This constraint, combining with Δr^* , will give a quite sensitive way to differentiate various inflationary type models. For the EPIC-LC, the uncertainty of n_t is about 2 times larger than that of EPIC-2m. When $r = 0.001$, we have $\Delta n_t = 0.10$, and when $r = 0.1$, we have $\Delta n_t = 0.02$.

It is necessary to discuss the contributions of S/N and Δn_t from every multipole, which can be very easily analyzed by the analytical formulae. From Eqs. (14) and (15), we find these two quantities can be rewritten as follows

$$(S/N)^2 = \sum_{\ell} \sum_Y a_{\ell}^{Y2}, \quad (1/\Delta n_t)^2 = \sum_{\ell} \sum_Y (a_{\ell}^Y b_{\ell}^*)^2. \quad (22)$$

They are the simple sums of the contributions from each multipole ℓ and CMB information channel Y . We plot the functions of $\sum_Y a_{\ell}^{Y2}$ and $\sum_Y (a_{\ell}^Y b_{\ell}^*)^2$ as a function of ℓ for two different models ($r = 0.01$ and $r = 0.1$). The results are shown in Fig. 4. Left panel shows that all these four lines are peaked at $\ell \sim 100$, which is close to the peak

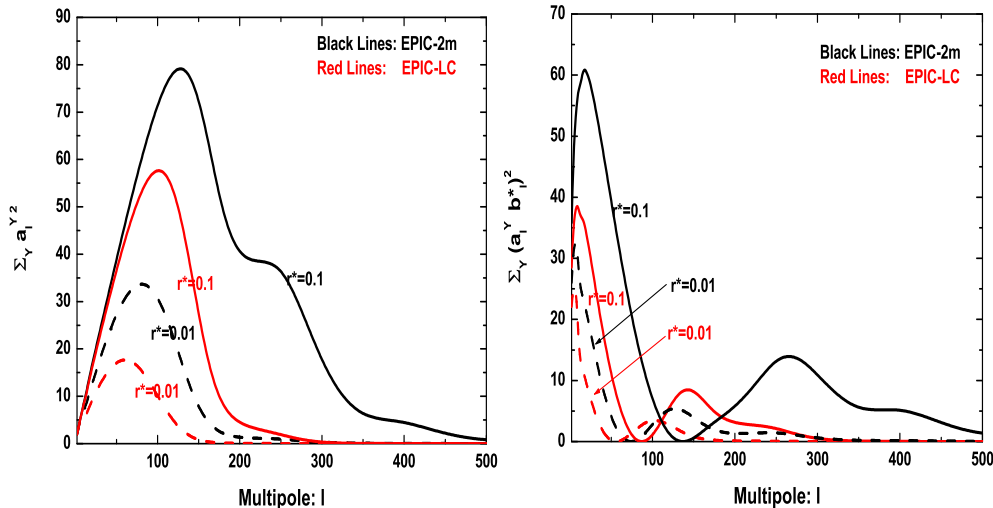


FIG. 4: The figures show the values of $\sum_Y a_\ell^{Y2}$ (left panel) and $\sum_Y (a_\ell^Y b_\ell^*)^2$ (right panel) as functions of multipole ℓ for the cases with the different r^* . Here, we have not considered the contaminations from cosmic weak lensing and foreground emissions.

of B -polarization. This reflects that when $r > 0.01$, the main contribution comes from the observation in the range $\ell \sim 100$, consistent with our previous discussion. This is different from the case of Planck satellite [18, 22], where the reionization peak at $\ell \sim 6$ is extremely important. In the CMBPol case, the contribution from the largest scale $\ell < 20$ is unimportant due to the cosmic variance, and the contribution from the small scale $\ell > 300$ is also unimportant for the large instrumental noises. However, it is important to mention that if $r \ll 0.01$, similar to Planck satellite, the reionization peak at $\ell < 10$ again becomes the main contribution for the total S/N .

However, it is different for $\sum_Y (a_\ell^Y b_\ell^*)^2$, which stands for the individual contribution for $1/\Delta n_t$. From the right panel of Fig. 4, we find that this function is sharply peaked at the largest scale $\ell < 30$, and the contribution from intermedial scale around the best-pivot multipole is very small. These can be easily understood, the quantity $b_\ell^* \equiv \ln(\ell/\ell_t^*)$ is zero when $\ell = \ell_t^*$, which follows that $\sum_Y (a_\ell^Y b_\ell^*)^2 = 0$ at $\ell = \ell_t^*$. Only if $\ell \ll \ell_t^*$ or $\ell \gg \ell_t^*$, b_ℓ^* has a large value, and follows a large $\sum_Y (a_\ell^Y b_\ell^*)^2$. Especially, the contribution from $\ell \ll \ell_t^*$ is very important. For example, when $\ell_t^* = 137$, $b_{\ell=2}^{*2}$ is 30 times large than $b_{\ell=300}^{*2}$. This reflects that the constraint on the tilt of the primordial gravitational waves power spectrum strongly depends on the observations in a large scale range. The cosmic reionization is very important for the constraint of n_t , although it might not be so important for the constraint of r for the CMBPol observations.

IV. COSMIC WEAK LENSING CONTAMINATION

In [13], it was pointed out that the gravitational waves result in CMB polarization with a B -mode, whereas density perturbations do not. Thus, the signal of gravitational waves could not be confused with density perturbations by detecting the B -polarization. Although, the amplitude of the B -polarization is expected to be quite small, it gives a clear information for gravitational waves. However, when taking into account the second-order effect, the B -mode can also arise from the lensing of the E -mode by density perturbations along lines-of-sight between the observer and the last-scattering surface [44]. The scalar contribution to the B -mode power spectrum is shown in Fig. 2 (grey dashed line). When $\ell < 200$, it is nearly a white spectrum with the amplitude $C_{\text{lens},\ell}^B \simeq 2 \times 10^{-6} \mu\text{K}^2$, which is 7 times larger than the instrumental noises of EPIC-2m, and 3 times larger than that of EPIC-LC.

When the instrumental noise of the CMB experiment is sufficiently small, as the CMBPol mission, the gravitational lensing contribution to the large-scale B -mode becomes one of the limiting sources of contamination for constraining

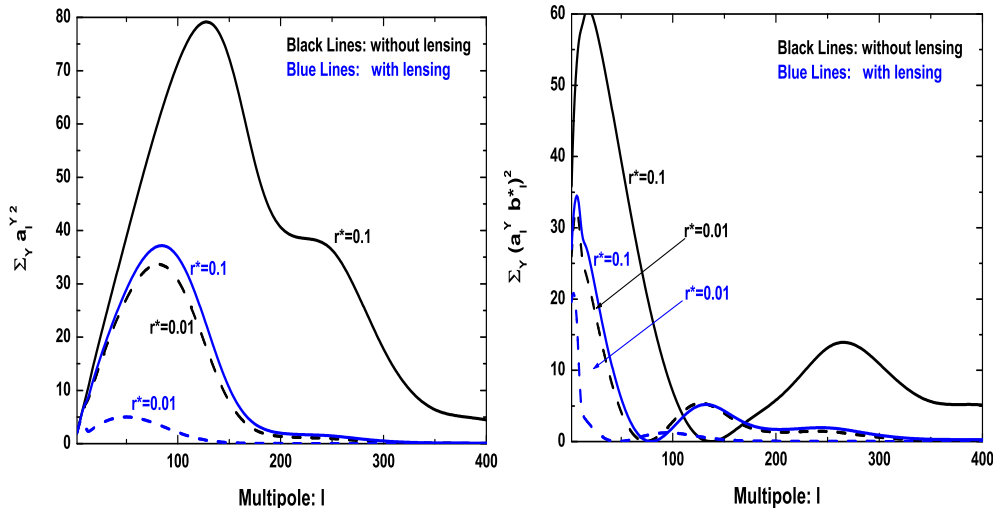


FIG. 5: For EPIC-2m, the figures show the values of $\sum_Y a_\ell^{Y^2}$ (left panel) and $\sum_Y (a_\ell^Y b_\ell^*)^2$ (right panel) as functions of multipole ℓ for the cases with and without the reduced cosmic lensing contamination with the residual factor $\sigma^{\text{lens}} = 0.5$.

the RGWs. High-sensitivity measurements of small-scale B -modes can reduce this contamination through a lens reconstruction technique, which has been discussed by a number of authors (see for instance [45–47]).

The effect of cosmic lensing contamination for the detection of RGWs can be easily discussed. The reduced lensed B -mode polarization can be treated simply as a well-known noise for gravitational waves in the likelihood analysis, i.e.

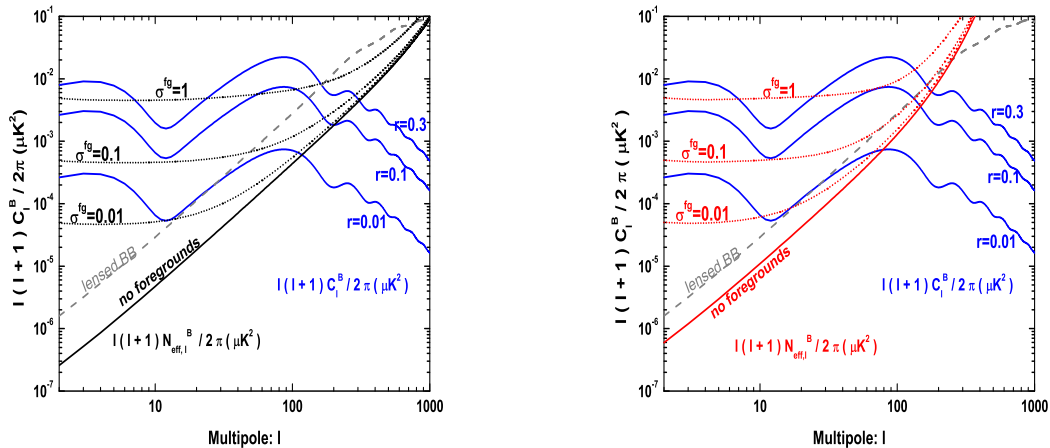
$$N_\ell^B \mapsto N_{\text{ins},\ell}^B + C_{\text{lens},\ell}^B \times \sigma^{\text{lens}}, \quad (23)$$

where we have defined the residual factor σ^{lens} for the lensed B -polarization. Note that in the real situation, the lens-induced B -modes are non-Gaussian, so we should not behave exactly it as the additional Gaussian noise (see [47] and references therein). However, on the scales relevant for B -mode detection in this paper, the non-Gaussianity has only a minor effect, which has been ignored in our discussion. In general, we have $\sigma^{\text{lens}} \leq 1$, with the equality holding for the lensed B -mode is not reduced. The reduction of gravitational lensing contribution strongly depends on the instrumental noise level, the beam FWHM, the foregrounds and the instrumental systematics. In the work [48], the authors found that, based on the noise level of EPIC-2m, one can expect to have $\sigma^{\text{lens}} \sim 0.5$. However, for EPIC-LC, it is very difficult to reduce the cosmic lensing contamination due to the large beam FWHM. We should mention that since the value of $C_{\text{lens},\ell}^B$ is much larger than the instrumental noises of CMBPol mission, in the total effective noise N_ℓ^B , the cosmic lensing contamination becomes the dominant portion.

We have calculated the constraints of the gravitational waves by taking into account the cosmic lensing contaminations. The values of ℓ_t^* , S/N and Δn_t are shown in Fig. 3, where $\sigma^{\text{lens}} = 0.5$ and $\sigma^{\text{lens}} = 1$ are considered for EPIC-2m, and $\sigma^{\text{lens}} = 1$ is considered for EPIC-LC. The left panel shows that, the best-pivot multipole is shifted to smaller scale by the lensing contamination. We find the value of S/N is much reduced by the lensing contamination, especially for the case with small tensor-to-scalar ratio. When $r = 0.001$, we have $S/N = 7$ for EPIC-2m (with $\sigma^{\text{lens}} = 0.5$) and $S/N = 4$ for EPIC-LC, which are much smaller than the corresponding values with only instrumental noises. The uncertainty of n_t is also much increased by the cosmic lensing, especially for the case with small r . When $r = 0.001$, EPIC-2m with $\sigma^{\text{lens}} = 0.5$ can give $\Delta n_t = 0.12$, and EPIC-2m with $\sigma^{\text{lens}} = 1$ can give $\Delta n_t = 0.16$, which are more than 2 times larger than those in the case without cosmic lensing, and are fairly loose to differentiate various inflationary models. However, when the tensor-to-scalar ratio is $r = 0.1$, we have $\Delta n_t = 0.02$ for EPIC-2m, which is

TABLE II: Assumptions about foreground emissions. [28]

Parameter	Synchrotron	Dust
$A_{S,D}$	$4.7 \times 10^{-5} \mu\text{K}^2$	$1.2 \times 10^{-4} \mu\text{K}^2$
ν_0	30 GHz	94 GHz
ℓ_0	350	900
α	-3	2.2
β^E	-2.6	-1.3
β^B	-2.6	-1.4
β^C	-2.6	-1.95


 FIG. 6: The total effective noise power spectra $N_{\text{eff},\ell}^B$ when considering the foreground contaminations. The left panel is for EPIC-2m and the right panel is for EPIC-LC.

still a quite tight constraint.

We have also investigated the contribution of every multipole for S/N and Δn_t . The results can be found in Fig. 5, where we have focused on the EPIC-2m mission and $\sigma^{\text{lens}} = 0.5$ is used for the case with cosmic lensing contamination. We find that the peak in each case is much reduced by the lensing contamination.

It is interesting to mention that for the high-sensitivity detectors the residual lensing noise dominates over the instrumental noises, and place the detection limit for CMB experiments [49]. In [46], the authors claimed that, for an extreme high-sensitivity detector, a reduction in lensing power by a factor 40 is possible using approximate iterative maximum-likelihood method. If we consider this residual as the lower limit of the reduced lensing noises, we find that $r > 3.7 \times 10^{-6}$ can be detected at more than $2\text{-}\sigma$ level in absence of sky cuts, foregrounds and instrumental systematics [24]. This can be treated as the detection limit of the CMB experiments for gravitational waves. This lower limit corresponds to the Hubble parameter $H \simeq 3.1 \times 10^{11} \text{ GeV}$, and the energy scale of inflation $V^{1/4} \simeq 1.5 \times 10^{15} \text{ GeV}$. In this limit case, the uncertainty of spectral index also becomes very small. When $r = 0.1$, we have $\Delta n_t = 0.007$ (see Fig. 2 in [24] for details), placing a very tight constraint on the inflationary models.

V. FOREGROUND CONTAMINATIONS

In this section, besides the instrumental noises and cosmic lensing contaminations, we shall take into account the impact of polarized foregrounds on the future CMBPol mission. In this paper, we shall neglect the effect of foregrounds on the CMB temperature, as the foreground cleaning is expected to leave a negligible contribution in the temperature

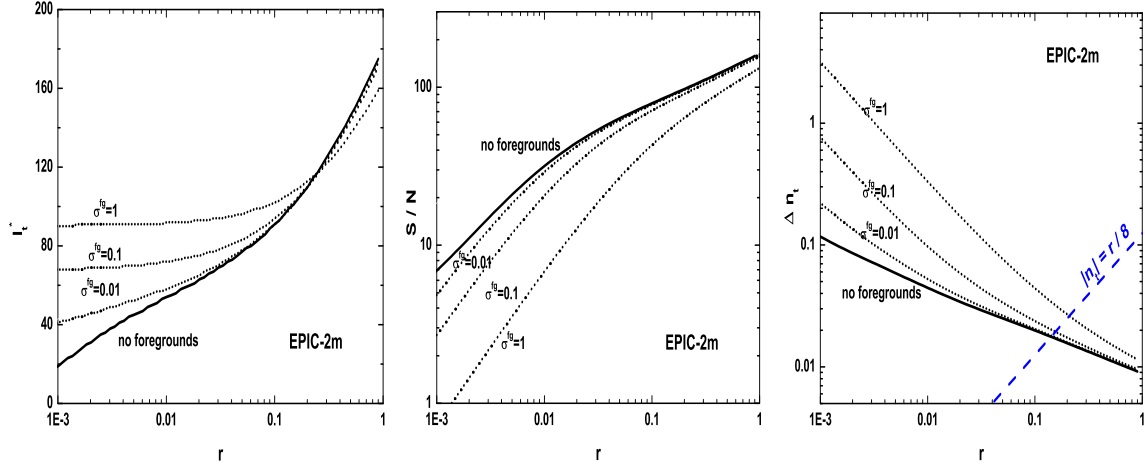


FIG. 7: This figure shows the values of ℓ_t^* , S/N and Δn_t depend on the foreground contaminations for EPIC-2m.

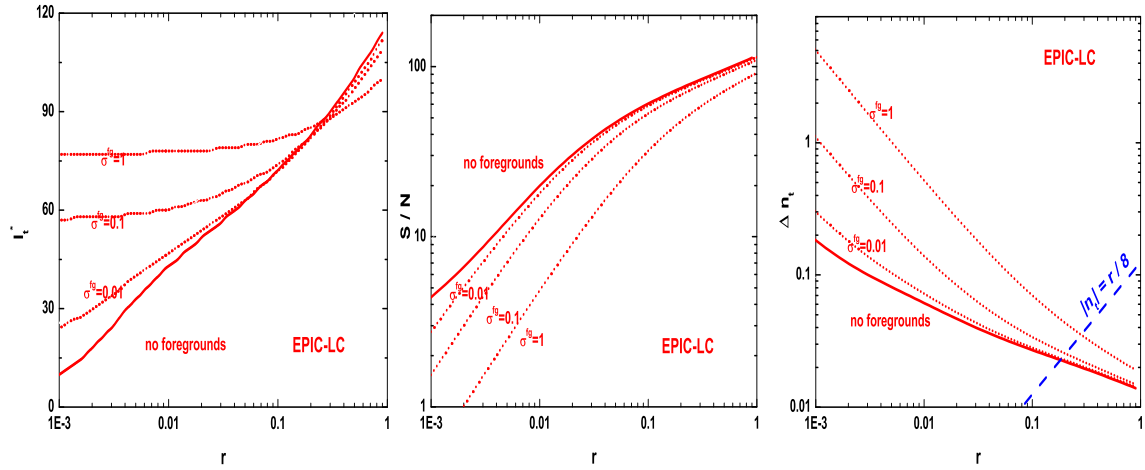


FIG. 8: This figure shows the values of ℓ_t^* , S/N and Δn_t depend on the foreground contaminations for EPIC-LC.

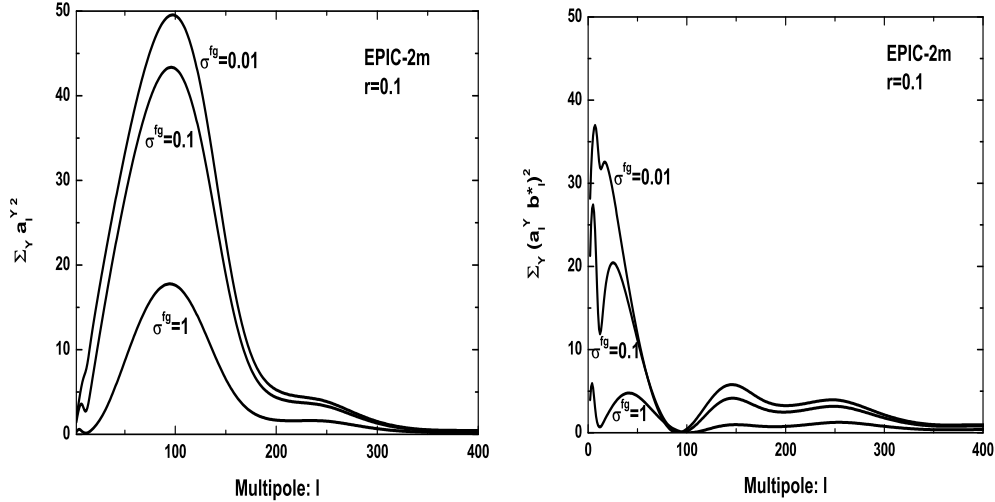


FIG. 9: The figures show the values of $\sum_Y a_\ell^Y{}^2$ (left panel) and $\sum_Y (a_\ell^Y b_\ell^{*Y})^2$ (right panel) as functions of multipole ℓ for the cases with different σ^{fg} .

[50]. CMB polarized foregrounds arise due to free-free, synchrotron, and dust emission, as well as due to extra-galactic sources such as radio sources and dusty galaxies. In this paper, we shall only consider only synchrotron and dust emission, which are expected to be dominant in the CMBPol frequency range [51].

The synchrotron emission results from the acceleration of cosmic-ray electrons in the magnetic field of Galaxy, which has been well measured on large angular scale at 23 GHz by WMAP. Following [28, 51, 52], for the frequency ν , the scale-dependence of the synchrotron signal may be parameterized as

$$C_{S,\ell}^Y(\nu) = A_S \left(\frac{\nu}{\nu_0} \right)^{2\alpha_S} \left(\frac{\ell}{\ell_0} \right)^{\beta_S^Y}. \quad (24)$$

The parameters in this formula for the various power spectra are all listed in Table II, where $\alpha_S = -3$ is assumed, β^E , β^B and β^C are the corresponding β_S^Y for synchrotron emissions. This choice matches the synchrotron emission at 23GHz observed and parameterized by WMAP [53], and agrees with the DASI measurements [54].

Galactic emission in the 100–6000 GHz frequency range is dominated by the thermal emission from warm interstellar dust grains. Our knowledge of polarized dust emission is relatively poor, which is expected to be characterized by the Planck satellite in the near future. In this paper, we shall adopt the parameterized formula for the dust emission at frequency ν as follows, as suggested by [28, 52],

$$C_{D,\ell}^Y(\nu) = p^2 A_D \left(\frac{\nu}{\nu_0} \right)^{2\alpha_D} \left(\frac{\ell}{\ell_0} \right)^{\beta_D^Y} \left[\frac{e^{h\nu_0/kT} - 1}{e^{h\nu/kT} - 1} \right]^2, \quad (25)$$

where $p = 5\%$ and $T = 18\text{K}$. We list the other parameters for the various power spectra in Table II.

Various methods have been discussed to subtract the foregrounds by their frequency-dependence (see for instance [55]). In this paper, we shall not discuss the subtraction of the foreground from the signal. Instead, as the previous works [28, 52] we assume that the foreground subtraction can be done correctly down to a given level, and treat these residual foregrounds as a kind of known gaussian noises in the data analysis. However, here we should mention that in this case we have assumed one can model and subtract the power spectra of residuals perfectly, and avoid the possible issues of bias. This might be a huge challenge for the future polarization observation.

If we consider the CMB experiment, including several frequency channels, and the different channels have different noise levels, the optimal channel combination gives the effective noise power spectra [28, 52]

$$[N_{\text{eff},\ell}^Y]^{-1} = \sum_i [N_{\text{fg},\ell}^Y(i) + N_{\text{ins},\ell}^Y(i)]^{-1}, \quad (26)$$

where i runs through the channels. $N_{\text{ins},\ell}^Y(i)$ is the instrumental noise power spectra of channel ν_i . $N_{\text{fg},\ell}^Y(i)$ is the residual foreground noises of channel ν_i , which is

$$N_{\text{fg},\ell}^Y(i) = \sum_{\text{fore}=\text{S,D}} C_{\text{fore},\ell}^Y(\nu_i) \sigma^{\text{fg}} + \mathcal{N}_{\text{fg},\ell}^Y(\nu_i). \quad (27)$$

Here, $C_{\text{fore},\ell}^Y$ is the model for the power spectrum of the synchrotron and dust signals at the frequency ν_i given by Eqs. (24) and (25), and σ^{fg} is the assumed residual factor. $\mathcal{N}_{\text{fg},\ell}^Y(\nu_i)$ is the noise power spectrum of the foreground template map, as foreground templates are created by effectively taking map differences and thus are somewhat affected by the instrumental noise. This term can be calculated by [28, 52]

$$\mathcal{N}_{\text{fg},\ell}^Y(\nu_i) = \frac{N_{\text{ins},\ell}^Y(\nu_{\text{ref}})}{n_{\text{chan}}(n_{\text{chan}} - 1)/4} \left(\frac{\nu_i}{\nu_{\text{ref}}} \right)^{2\alpha}, \quad (28)$$

where n_{chan} is the total number of channels used, and the reference channel ν_{ref} is the highest and lowest frequency channel included in the cosmological analysis for dust and synchrotron respectively, i.e., that listed in Table I. The parameters α for the foregrounds under consideration are defined in Table II, i.e. $\alpha = -3$ for the synchrotron emissions and $\alpha = 2.2$ for the dust emission. The quantity $N_{\text{ins},\ell}^Y(\nu_{\text{ref}})$ is the white instrumental noise (without the beam window function) of the corresponding template channel [52].

Thus the total noise power spectra, by combining the multipole-frequency instrumental noises and the residual foregrounds, as well as the residual cosmic lensing contamination, are given by

$$N_{\ell}^X \mapsto N_{\text{eff},\ell}^X (X = T, C, E), \quad N_{\ell}^B \mapsto N_{\text{eff},\ell}^B + C_{\text{lens},\ell}^B \times \sigma^{\text{lens}}, \quad (29)$$

where σ^{lens} is the residual factor for cosmic lensing contamination. In this and the following sections, we adopt $\sigma^{\text{lens}} = 0.5$ for EPIC-2m, and $\sigma^{\text{lens}} = 1$ for EPIC-LC. The effective noise power spectra $N_{\text{eff},\ell}^Y$ strongly depend on the residual factor σ^{fg} for the foregrounds. When no foreground subtraction is assumed, we have $\sigma^{\text{fg}} = 1$. In this paper, we also consider two assumed residual cases, suggested by CMBPol team [28]: $\sigma^{\text{fg}} = 0.01$ for the optimistic case, and $\sigma^{\text{fg}} = 0.1$ for the pessimistic case. In Fig. 6, we plot the effective noise power spectrum $N_{\text{eff},\ell}^B$ with different σ^{fg} for EPIC-2m (left panel) and EPIC-LC (right panel). We find that for both EPIC-2m and EPIC-LC, the foregrounds increase the effective noise power spectrum in all the multipole range when $\sigma^{\text{fg}} = 1$. However, when the foregrounds can be well subtracted, the residual foregrounds only increase the noise in the large scale. For $\sigma^{\text{fg}} = 0.1$, the effective noise is increased in the range $\ell < 300$, and for $\sigma^{\text{fg}} = 0.01$, the effective noise is increased in the range $\ell < 100$. We find that even if the optimistic case with $\sigma^{\text{fg}} = 0.01$ is realized, the effective noise is much larger in the reionization peak ($\ell < 20$) comparing with the no foreground case. Especially, when r is small, this increased noise is larger than the signal C_{ℓ}^B , and decreases the contribution of the reionization peak. We have emphasized above, the reionization peak is very important for the constraint of spectral index n_t for the CMBPol mission, it is predictable that the value of Δn_t would become much larger due to the foreground contaminations, even if the optimistic case is considered. This will be clearly shown in the following discussion.

By using the total effective noise power spectra in (29), we can calculate the values the best-pivot multipole ℓ_t^* , the signal-to-noise ratio S/N , and the uncertainty of the spectral index Δn_t . In Fig. 7 and Fig. 8, we show the results for EPIC-2m and EPIC-LC, respectively. We find that so long as $r < 0.3$, the value of ℓ_t^* is increased with the increasing of the residual foregrounds. This is because that, the contaminations from foreground are mainly in the low multipole (see Fig. 6). Increasing the foregrounds, the contribution for the detection of RGWs in the low multipoles becomes less and less important, induces an increasing of ℓ_t^* .

From Fig. 7 and Fig. 8, we find that when $\sigma^{\text{fg}} = 0.01$, the optimistic case we considered, the foregrounds decrease the S/N and increase Δn_t , when the tensor-to-scalar ratio $r < 0.03$. However, when $r > 0.03$, the effect of this residual foregrounds is negligible. This is also easily understood. The residual foregrounds with $\sigma^{\text{fg}} = 0.01$ only increase the total noise power spectra in the largest scale $\ell < 100$. This increased total noises are beyond the signals when r is small. We also find that, when $\sigma^{\text{fg}} = 0.1$ or $\sigma^{\text{fg}} = 1$, i.e. the foregrounds are not well subtracted, the effect of the foreground contaminations are quite important, especially for the determination of n_t . With the decreasing of r , the contaminations become more and more important. For the EPIC-2m and the input model with $r = 0.1$, when

$\sigma^{\text{fg}} = 0.01$, we have $\Delta n_t = 0.020$. When $\sigma^{\text{fg}} = 0.1$, the value becomes $\Delta n_t = 0.024$, and when $\sigma^{\text{fg}} = 1$, the value becomes $\Delta n_t = 0.045$, two times larger than that in the optimistic case. We can investigate another case, for the EPIC-2m and the input model with $r = 0.01$, when $\sigma^{\text{fg}} = 0.01$, we have $\Delta n_t = 0.054$. When $\sigma^{\text{fg}} = 0.1$, the value becomes $\Delta n_t = 0.098$, and when $\sigma^{\text{fg}} = 1$, the value becomes $\Delta n_t = 0.330$, six times larger than that in the optimistic case. So we conclude that if the value of r is not too small, such as $r = 0.1$, we do not need to remove the foreground to a very high level. The difference between optimistic case and pessimistic is very small. However, if the value of r is smaller than 0.01, very detailed removal for the foregrounds is very important for the determination of RGWs.

Fig. 7 and Fig. 8 also show that in the optimistic case, EPIC-2m can detect the signal of RGWs with $r = 0.001$ at $5\text{-}\sigma$ level, and EPIC-LC can detect it at $3\text{-}\sigma$ level. However, in the pessimistic case, EPIC-2m can only detect this signal at $2.8\text{-}\sigma$ level, and EPIC-LC can detect it at $1.6\text{-}\sigma$ level.

As in the previous sections, we can discuss the contribution to the S/N and Δn_t from the individual multipole, by investigating the functions $\sum_Y a_\ell^{Y2}$ and $\sum_Y (a_\ell^Y b_\ell^*)^2$. They are plotted in Fig. 9, where we have considered the EPIC-2m, and the model with $r = 0.1$. We find that the foreground contamination mainly affects the S/N by decreasing the value of $\sum_Y a_\ell^{Y2}$ around the peak at $\ell \sim 100$. However, it affects the value of Δn_t mainly by decreasing of $\sum_Y (a_\ell^Y b_\ell^*)^2$ at the largest scale $\ell < 50$ and the intermedial range $\ell \sim 200$.

Now, let us investigate the possible application of the CMBPol mission to differentiate the different inflationary models, which plays a role for the future inflation researches. As well known, one of the most important ways to distinguish different classes of inflations is to test the so-called inflationary consistency relations. This testing strongly depends on the determination of the parameters specifying the relic gravitational waves, i.e. the tensor-to-scalar ratio r and the spectral index n_t . Now, let us focus on the possible testing of the consistency relation for the canonical single-field slow-roll inflationary models [10]. This testing might provide the unique model-independent criteria to confirm or rule out this class of models. The possible testing for other inflationary models by the CMBPol mission and the ideal CMB experiment can be found in the recent work [56].

The consistency relation for the canonical single-field slow-roll inflationary models can be written as [10]

$$r = -8n_t. \quad (30)$$

We find that this relation only depends on the parameters r and n_t . Since the absolute value of n_t is expected to be one order smaller than that of r , and also the measurement of n_t is much more difficult than r , how well we can measure the spectral index n_t plays a crucial role for testing the consistency relation in Eq. (30).

To access whether CMBPol mission might achieve the consistency relation test goal, in Fig. 7 and Fig. 8 (right panels), we compare the values of $|n_t| = r/8$ with Δn_t . If $\Delta n_t < |n_t|$, then the constraint on n_t is tight enough to allow for the testing. From Fig. 7, we find that for the EPIC-2m mission, $\Delta n_t < |n_t|$ is satisfied only if $r > 0.14$ for the optimistic case with $\sigma^{\text{fg}} = 0.01$. In the pessimistic case with $\sigma^{\text{fg}} = 0.1$, it becomes $r > 0.15$. Similar results for the EPIC-LC can be found in Fig. 8. $\Delta n_t < |n_t|$ is satisfied only if $r > 0.18$ for the optimistic case, and $r > 0.20$ for the pessimistic case. So we conclude that the testing of the consistency relation for the canonical single-field slow-roll by the CMBPol mission is quite hard. The testing is possible only for some large-field inflationary models. However, we should mention that the situation could become quite promising for the general Lorentz-invariant single-field inflations and the two-field inflations (see [56] for the details).

VI. SYSTEMATICS CONTAMINATIONS

Beyond raw sensitivity requirements for the instrumentals, and the removal of the astrophysical foregrounds, much attention has already been given in the literature to the instrumental systematics for the constraints of the cosmological parameters and the cosmic weak lensing reconstruction [57–60]. The main goal of this section is to illustrate the effect of the instrumental systematics and systematically study the impact on the gravitational waves detection for the CMBPol mission.

All the effects of the beam systematics are associated with beam imperfections or beam mismatch in dual beam experiments. Several of these effects (e.g. differential gain, differential beam width and the first order pointing error) are reducible with an ideal scanning strategy and otherwise can be cleaned from the data set. Other spurious polarization signals, such as those due to differential ellipticity of the beam, second order pointing errors and the differential rotation, persist even in the case of ideal scanning strategy and perfectly mimic CMB polarization.

The beam systematics due to optical imperfections are dependent of the underlying sky, the properties of the polarimeter and the scanning strategy. If the outputs of two beams with orthogonal polarization-sensitive directions are slightly different, the temperature anisotropy can leak to the polarization or the E -mode polarization can leak to the B -mode and vice versa. (see [59] for the details). For example, if two beams are exactly same but the overall response, this difference of the measured intensity can generate a non-vanishing polarization signal. Another typical

example is effect of the beam rotation, which is caused by the uncertainty in the overall beam orientation. This effect mixes the Stokes parameters Q and U , and induces a E -mode and B -mode leakage.

The CMB power spectra $C_{\text{sys},\ell}^Y$ generated by these systematics are discussed in details by a number of authors. In the work [59], the authors discussed these effects separately, and got the simple analytical formulas to calculate the leading order of the generated power spectra, which are listed in Table III. The formulae in Table III separately describe the effects of the following instrumental systematics for experiments with the elliptical gaussian beams: differential gain effect, monopole effect, differential pointing effect, quadrupole effect, differential rotation effect. Differential gain can induce spurious polarization singles from temperature leakage due to beam mismatch. This effect is described by the parameter $g \equiv g_1 - g_2$, where g_1 and g_2 refer to the gain factors of first and second beams. The differential rotation effect is due to uncertainty in the overall beam orientation. This mixes the Q and U Stokes parameters and as a result leaks E to B and vice versa. We describe this effect by the parameter $\varepsilon \equiv (\varepsilon_1 + \varepsilon_2)/2$, where ε_1 and ε_2 are rotation errors of first and second beams. We note that these two parameters g and ε are not related to the beam shape. The monopole effect arises from circular beams with unmatched main-beam full width at half maximum, which is described by the parameter $\mu \equiv (\sigma_1 - \sigma_2)/(\sigma_1 + \sigma_2)$, where σ_1 and σ_2 are the mean beamwidths of first and second beams. The quadrupole effects arises from beams with differential ellipticities, and described by the ellipticity parameter $e \equiv (\sigma_x - \sigma_y)/(\sigma_x + \sigma_y)$, where σ_x and σ_y are the major and minor axes of the beam. Also, differential pointing, i.e. the dipole effect, is described the parameter $\rho \equiv \rho_1 - \rho_2$, where ρ_1 and ρ_2 are the circular positions of first and second beams. These three effects can induce future spurious polarization singles from temperature leakage.

In the formulae in Table III, the functions f_1 , f_2 and f_3 are experiment-specific and encapsulate the information about the scanning strategy which couples to the beam mismatch parameters to generate spurious polarization. The exact definitions of f_1 , f_2 and f_3 are given in Eq. (27) in [59], i.e.

$$f_1 = \frac{1}{2}|\tilde{h}_+(-1, 0)|^2, \quad f_2 = \frac{1}{2}|\tilde{h}_+(-1, -1)|^2 + \frac{1}{2}|\tilde{h}_+(-1, 1)|^2, \quad f_3 = \frac{1}{2}\langle \tilde{f}(0, 1)\tilde{h}_-^*(1, -1) \rangle,$$

where

$$f(m, n) \equiv \langle e^{-i(2m+n)\alpha} \rangle, \quad h_{\pm} \equiv \frac{1}{D}[f(m, n) - f(m \pm 2, n)\langle e^{\pm 4i\alpha} \rangle], \quad D \equiv 1 - \langle e^{4i\alpha} \rangle \langle e^{-4i\alpha} \rangle.$$

$\tilde{f}(m, n)$ and $\tilde{h}_{\pm}(m, n)$ are the Fourier transformations of $f(m, n)$ and $h_{\pm}(m, n)$. Exact definition of α can be found in [59]. Angular brackets represent average over measurements of a single pixel, averaged over time. In general, these functions are spatially-anisotropic but for simplicity, and to obtain a first-order approximation, we consider them constants in general.

In the real data analysis, these generated CMB power spectra may be treated as a part of the signals, as well as the real signals generated by the perturbations fields, i.e.

$$C_{\ell}^Y \mapsto C_{\ell}^Y + C_{\text{sys},\ell}^Y. \quad (31)$$

Thus the estimator of this contamination D_{ℓ}^Y becomes biased for the true power spectra C_{ℓ}^Y , by a term $C_{\text{sys},\ell}^Y$. And this biased estimator will induce the biased estimator for the cosmological parameters in the likelihood analysis. As in general, we can use the r_{ML}^* and $n_{t\text{ML}}$ as the best estimator for the parameters r^* and n_t . Following the previous works [60], we define the bias of the tensor-to-scalar ratio δr and the spectral index δn_t as follows,

$$\delta r \equiv \langle r_{\text{ML}}^* \rangle - r^*, \quad \delta n_t \equiv \langle n_{t\text{ML}} \rangle - n_t. \quad (32)$$

Given the beam systematics the bias of the tensor-to-scalar ratio δr and the spectral index δn_t can be calculated by the following formulae (similar to the previous works [60]),

$$\delta r = r^* \frac{\sum_{\ell} \sum_Y a_{\ell}^Y e_{\ell}^Y}{\sum_{\ell} \sum_Y a_{\ell}^{Y2}}, \quad \delta n_t = \frac{\sum_{\ell} \sum_Y a_{\ell}^Y e_{\ell}^Y b_{\ell}^*}{\sum_{\ell} \sum_Y (a_{\ell}^Y b_{\ell}^*)^2}, \quad (33)$$

where $e_{\ell}^Y \equiv C_{\ell}^Y(\text{sys})/\sigma_{D_{\ell}^Y}$. Notice that, for the requirement of the beam systematics of CMBPol mission (for instant, the parameter g , associated with the differential gains, satisfies $g \ll 0.01\%$ [48]), the power spectra generated by the beam systematics are expected to be much smaller than those generated by gravitational waves with $r > 10^{-3}$ but the very large multipole range, where the noises are dominant. So beam systematics cannot change the value of the best-pivot multipole.

Considering the CMB experiment with multi-frequency channels, the effective combined noise power spectra in Eq. (26) can be extended to the follows, considering the contribution of the systematics,

$$[N_{\text{eff},\ell}^Y]^{-1} = \sum_i [N_{\text{fig},\ell}^Y(i) + N_{\text{ins},\ell}^Y(i) + C_{\text{sys},\ell}^Y(i)]^{-1}, \quad (34)$$

where i runs through the channels. Throughout this section, we shall assume the optimistic foreground removal with the residual factor $\sigma^{\text{fg}} = 0.01$ for both EPIC-2m and EPIC-LC missions. We should remember that, similar to the previous discussion, the B -mode contamination ($\sigma^{\text{lens}} = 0.5$ for EPIC-2m, and $\sigma^{\text{lens}} = 1$ for EPIC-LC) by weak lensing effect is also considered throughout this section. The total CMB power spectra generated beam systematics can be calculated by $C_\ell^Y(\text{sys}) = N_{\text{eff},\ell}^Y(\text{with sys}) - N_{\text{eff},\ell}^Y(\text{no sys})$. In the simplest case with single frequency channel, this term returns to $C_\ell^Y(\text{sys}) = C_{\text{sys},\ell}^Y$.

Let us separately investigate the five systematical effects. Fig. 10 shows $C_\ell^B(\text{sys})$ for different values of the parameter $g = 0.002\%$, 0.005% and 0.01% . In all these figures, $f_1 = 2\pi$ is used as the worst case. The values of $\ell(\ell+1)C_\ell^B(\text{sys})$ only weakly depends on the multipole ℓ . As long as $r > 0.01$, we find $C_\ell^B(\text{sys})$ are all smaller than those of the signals C_ℓ^B or the noises $N_{\text{eff},\ell}^B$ in the range $\ell < 200$. In Fig. 11, we plot the values of biases δr and δn_t induced by the differential gains. We find that the values of δr and δn_t strongly depends on the value of the parameter g . A larger g follows a larger bias. However, the uncertainties Δr and Δn_t are nearly independent of g unless the value of g is too large. We also find that, given the parameter g the value of the ratio $\delta r/\Delta r$ also strongly depend on the tensor-to-scalar ratio r . For example, the EPIC-2m experiment with $g = 0.01\%$, δr is larger than Δr when $r < 0.04$, the bias is very obvious. However when $r > 0.04$, we have $\delta r < \Delta r$, the bias is smaller than the uncertainty.

Similar to the previous work [60], we can define the critical value g_c , which is the largest value of g as long as the condition $\delta r/\Delta r < 0.1$ is satisfied. In Table IV, we list the critical values of g_c for EPIC-2m and EPIC-LC, where $r = 0.001$, 0.01 and $r = 0.1$ are considered. Since Fig. 11 shows that for a given g value, both Δr and δr increase with the increasing of r . So the tendency of the critical g_c for different input r is not trivial. After analysis, we find that for the assumed g value, with the increasing of r , if the increasing of Δr is more rapid than that of δr , thus the case with larger r corresponds to a larger g_c . This is clearly shown in Table IV. On the other hand, if the increasing of δr is more rapid than that of Δr , thus the case with larger r corresponds to a smaller g_c . Similar discussion is also applied to the n_t case, as well as the cases for the other four systematics contaminations. From Table IV, we find the severest constraints are obtained from the requirement of the small r case. The requirement for EPIC-2m is quite close to that of EPIC-LC.

Let us discuss the effect of beam gain on the determination of spectral index n_t . From Eq. (33), we find that the bias e_ℓ^Y in the lower multipole range $\ell < \ell_t^*$ contributes a negative δn_t , and the bias e_ℓ^Y in the high multipole range $\ell > \ell_t^*$ contributes a positive δn_t . These two components are cancelled by each other and total bias δn_t is expected to be very small, which is clearly shown in Fig. 11 (right panel). Comparing with the bias of r , the bias δn_t is much smaller than that of Δn_t . So the constraint on g obtained from the requirement of the n_t is much larger than that from the parameter r .

Now, let us turn to the effect of the differential monopole effect. From the formulae in Table III we know the power spectra generated by differential monopole effect strongly depend on the beam size. Larger beam size follows the larger power spectra $C_{\text{sys},\ell}^Y$. This can be seen clearly in Fig. 12. Given $\mu = 0.1\%$, the value of $C_\ell^B(\text{sys})$ is much larger in EPIC-LC than that in EPIC-2m. So in order to achieve a same value of $\delta r/\Delta r = 0.1$, the requirement for EPIC-LC is much severer than that for EPIC-2m, which are clearly shown in Table IV. Fig. 13 shows that, for a given μ , a larger r follows a larger ratio value $\delta r/\Delta r$, which is correct for both EPIC-2m and EPIC-LC. In order to keep the tensor-to-scalar ratio in the range $r \in (0.001, 0.1)$ unbiased, we should have $\mu_c = 0.029\%$ for EPIC-2m, and $\mu_c = 0.005\%$ for EPIC-LC, where $f_1 = 2\pi$ is adopted. we can also discuss the effect of differential monopole on the determination of spectral index n_t . From Fig. 12, we find that $C_{\text{sys},\ell}^Y$ is sharply peaked at the high multipole, where $\ell > \ell_t^*$. Thus the total contribution to δn_t is always positive (see Fig. 13), especially when the value of μ is not too small, the effect of differential monopole at the small scale is very important, and follows a fairly large bias for spectral index. Let us define the value of μ_c , where $\delta n_t/\Delta n_t = 0.1$ is satisfied. From Table IV we find that the constraint on μ is a little severer from the parameter n_t than that from the parameter r . This table shows that, the most severe constraint on μ is obtained from the requirement of n_t in the case of $r = 0.1$.

In Figs. 14 and 15, we show the effect of differential pointing on the determination of gravitational waves, where $f_2 = 2\pi$ is adopted. These figures show that similar with the case of differential monopole effect, the function $C_\ell^B(\text{sys})$ generated by differential pointing is also sharply peaked at the high ℓ , which follows that the bias of the spectral index δn_t is positive. Comparing the left panel with the right panel in Fig. 14, we find that for a given ρ , the effect of the differential pointing is more important for the EPIC-2m, due to the smaller instrumental noises. So more severe constraint on the differential pointing is followed for the EPIC-2m. In Table IV, we find that for both EPIC-2m and EPIC-LC, the most severe on ρ comes from the requirement of parameter n_t at $r = 0.1$.

We have also investigated the effect of the differential quadrupole in Figs. 16 and 17. The effects are similar to those of the differential monopole. We find that EPIC-LC needs the much stricter requirement than EPIC-2m. For each experiment, the most severe constraint on the parameter e is obtained from the requirement of n_t in the case with $r = 0.1$.

At last, we shall discuss the effect of the differential rotation, and the results are shown in Figs. 18 and 19. We

TABLE III: The leading order contributions of the systematic effects to the CMB power spectra, assuming the underlying sky is not polarized (except for the rotation signal) [59], where $z \equiv (\ell\sigma)^2 e$ and σ is mean beamwidth of the beam, which is calculated by $\sigma = \theta_F / \sqrt{8 \ln 2}$. $c_\theta \equiv \cos(\theta)$, where θ is the angle between ellipse major axis of the elliptical gaussian beam and the horizontal x -axis of the fixed focal plane. $c_\psi \equiv \cos(\psi)$ and $s_\psi \equiv \sin(\psi)$, where ψ is the angle between the axis of polarization sensitivity and the major axis of the elliptical beam. A clear show of the angles θ and ψ can be found in Fig. 1 in [59]. The definitions of the other parameters can be found in the text, see also [59].

Effect	Parameter	$C_{\text{sys},\ell}^C$	$C_{\text{sys},\ell}^B$	$C_{\text{sys},\ell}^B$
Gain	g	0	$g^2 f_1 C_\ell^T$	$g^2 f_1 C_\ell^T$
Monopole	μ	0	$4\mu^2 (\ell\sigma)^4 C_\ell^T f_1$	$4\mu^2 (\ell\sigma)^4 C_\ell^T f_1$
Pointing	ρ	$-c_\theta J_1^2(\ell\rho) C_\ell^T f_3$	$J_1^2(\ell\rho) C_\ell^T f_2$	$J_1^2(\ell\rho) C_\ell^T f_2$
Quadrupole	e	$-I_0(z) I_1(z) c_\psi C_\ell^T$	$I_1^2(z) c_\psi^2 C_\ell^T$	$I_1^2(z) s_\psi^2 C_\ell^T$
Rotation	ε	0	$4\varepsilon^2 C_\ell^B$	$4\varepsilon^2 C_\ell^B$

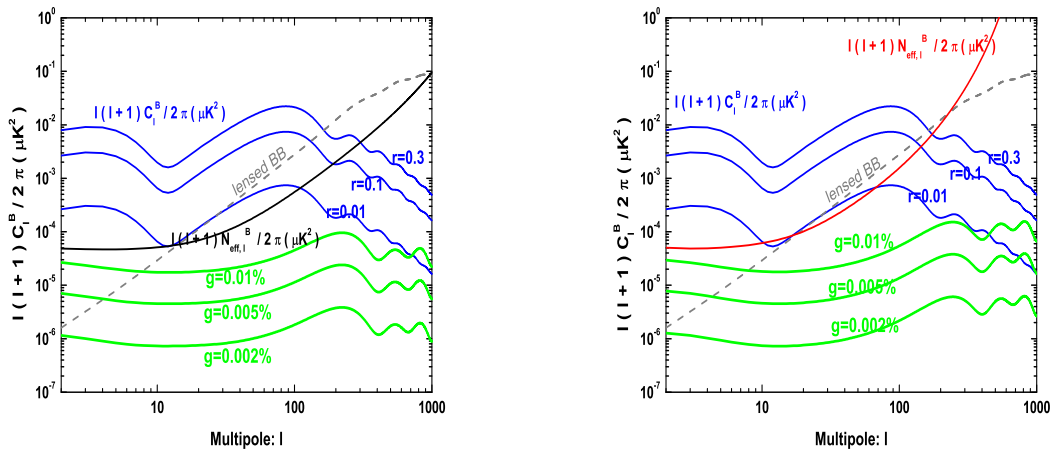


FIG. 10: The contribution of differential gain to the B -polarization, comparing with the signal of C_ℓ^B for different r , the noise of CMBPol mission, and the lensed B -polarization. Left panel is for EPIC-2m, and the right panel is for EPIC-LC.

find that for a given ε , the ratios $\delta r / \Delta r$ and $\delta n_t / \Delta n_t$ only weakly depend on the tensor-to-scalar ratio. And the ratio for EPIC-2m is a little smaller than that of EPIC-LC. In order to keep the parameters r and n_t unbiased, the requirement $\varepsilon < 0.09^\circ$ is needed for EPIC-2m, and $\varepsilon < 0.15^\circ$ is needed for EPIC-LC.

As a conclusion, by analyzing the effects of the systematics on the determination of gravitational waves, we find that the requirement of n_t unbiased follows the similar or even more severe constraints for the beam systematical parameters. For the effects of differential monopole, pointing and quadrupole, a larger r follows a more severe constraint for the systematics. The critical values for the systematical parameters are listed in Table IV, where the bold entries denote the most severe constraint in each case. We also find that comparing with EPIC-2m, the low cost EPIC-LC experiment has a much high requirement for the systematical parameters μ and e .

VII. CONCLUSION

The proposed CMBPol mission is the next generation of the space-based CMB experiment, which will survey the full sky and has the much smaller instrumental noises than Planck satellite. As one the most important tasks of this mission, detecting relic gravitational waves will be achieved if the tensor-to-scalar ratio $r \gtrsim 0.001$, which will provide a great opportunity to study the physics in the early Universe, especially in the inflationary stage.

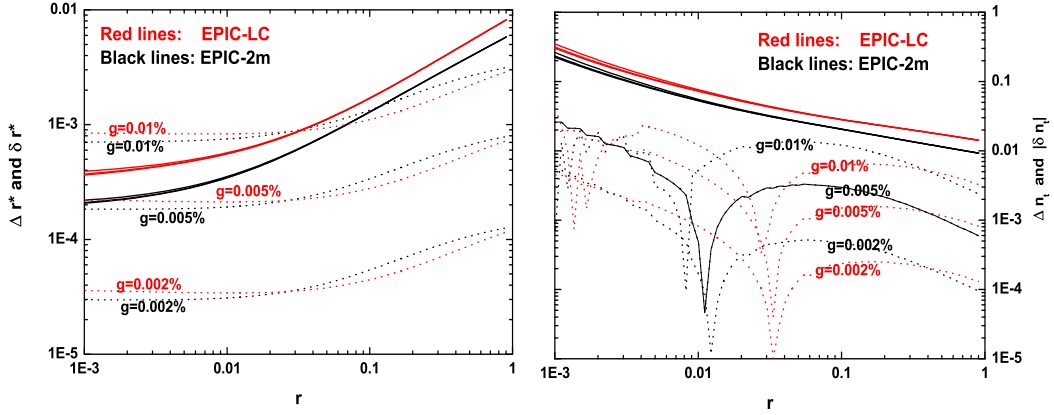


FIG. 11: The values of δr (left panel) and δn_t (right panel) from the differential gain for different tensor-to-scalar ratio r . For the comparison, we plot the corresponding Δr and Δn_t in solid lines in the panels.

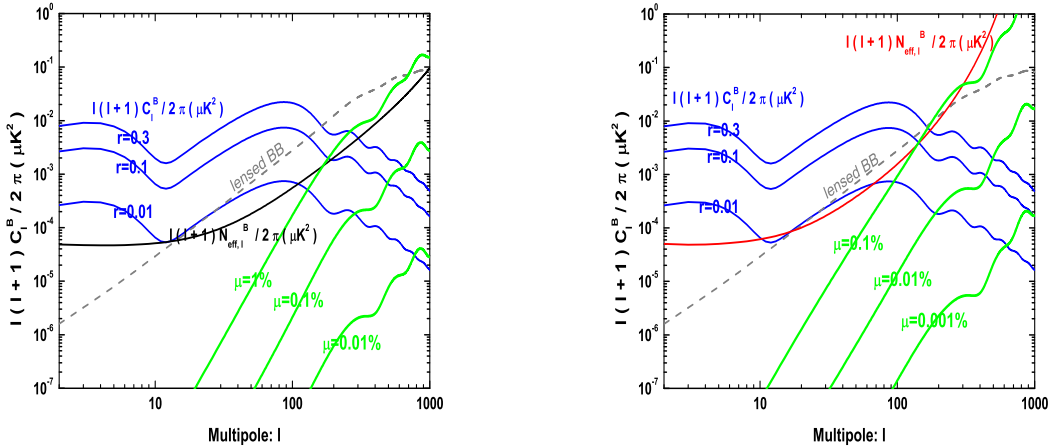


FIG. 12: The contribution of monopole effect to the B -polarization, comparing with the signal of C_ℓ^B for different r , the noise of CMBPol mission, and the lensed B -polarization. Left panel is for EPIC-2m, and the right panel is for EPIC-LC.

In this paper, we have detailedly discussed the detection of relic gravitational waves by focusing on the constraints of the parameters r and the spectral index n_t , which are always used to describe the primordial power spectrum of gravitational waves. In our discussion, we deeply investigate various contaminations for the detection, including the instrumental noises of CMBPol mission, the cosmic lensing contamination, the foreground contaminations, and the effect of various beam systematics. We found that the cosmic lensing becomes the dominant noise sources, comparing the instrumental noises for both EPIC-2m and EPIC-LC projects. Different from Planck satellite, if $r > 0.01$, the detection of gravitational waves mostly depends on the observation at multipole $\ell \sim 100$, the peak of the B -mode polarization. However, the reionization peak at $\ell \sim 10$ still plays a crucial role for the determination of spectral index

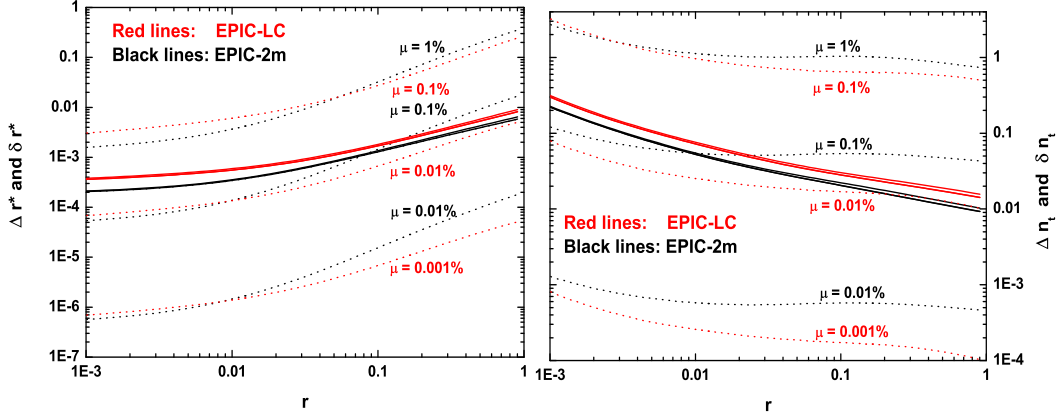


FIG. 13: The values of δr (left panel) and δn_t (right panel) from the monopole effect for different tensor-to-scalar ratio r . For the comparison, we plot the corresponding Δr and Δn_t in solid lines in the panels.

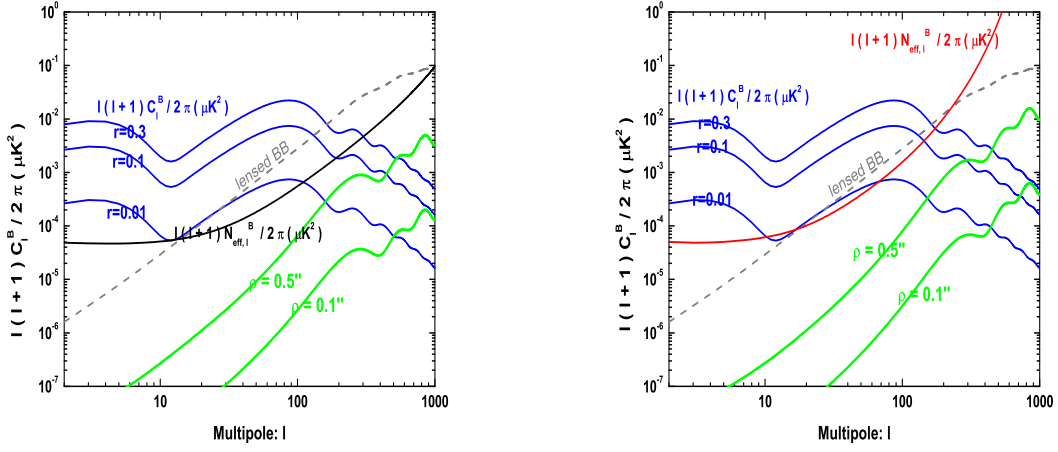


FIG. 14: The contribution of differential pointing to the B -polarization, comparing with the signal of C_ℓ^B for different r , the noise of CMBPol mission, and the lensed B -polarization. Left panel is for EPIC-2m, and the right panel is for EPIC-LC.

n_t . We also found that if the foreground contaminations cannot be well controlled, the reionization peak may be unobservable, which could deeply increase the uncertainty of n_t . At the same time, we have investigated the effect of various beam systematics on the detection of gravitational waves, which mainly cause a bias on the cosmological parameters. In order to keep these biases small enough, the requirements for the beam systematical parameters are quite severe, especially for the EPIC-LC mission.

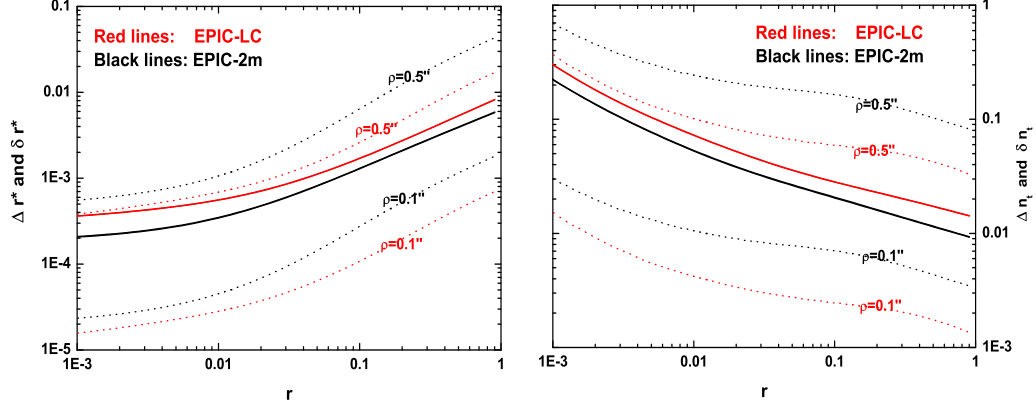


FIG. 15: The values of δr^* (left panel) and δn_t (right panel) from the differential pointing for different tensor-to-scalar ratio r . For the comparison, we plot the corresponding Δr and Δn_t in solid lines in the panels.

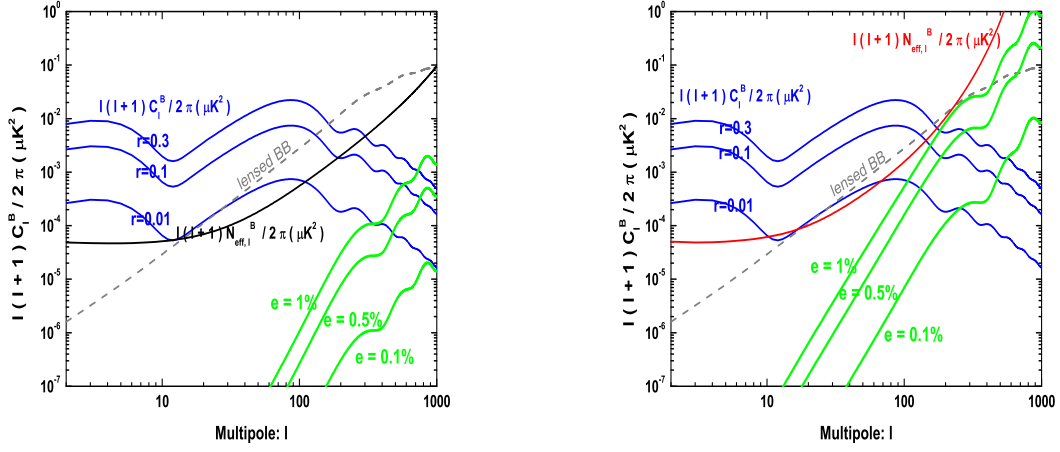


FIG. 16: The contribution of quadrupole effect to the B -polarization, comparing with the signal of C_l^B for different r , the noise of CMBPol mission, and the lensed B -polarization. Left panel is for EPIC-2m, and the right panel is for EPIC-LC.

Acknowledgements

The author is partially supported by Chinese NSF Grants No. 10703005, No. 10775119, No. 11075141. We thank the anonymous referee for the useful comments and suggestions.

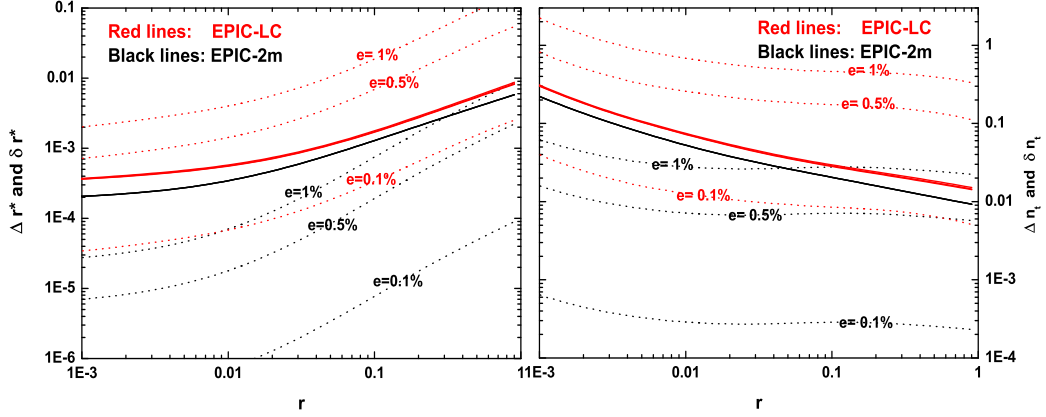


FIG. 17: The values of δr^* (left panel) and δn_t (right panel) from the quadrupole effect for different tensor-to-scalar ratio r . For the comparison, we plot the corresponding Δr and Δn_t in solid lines in the panels.

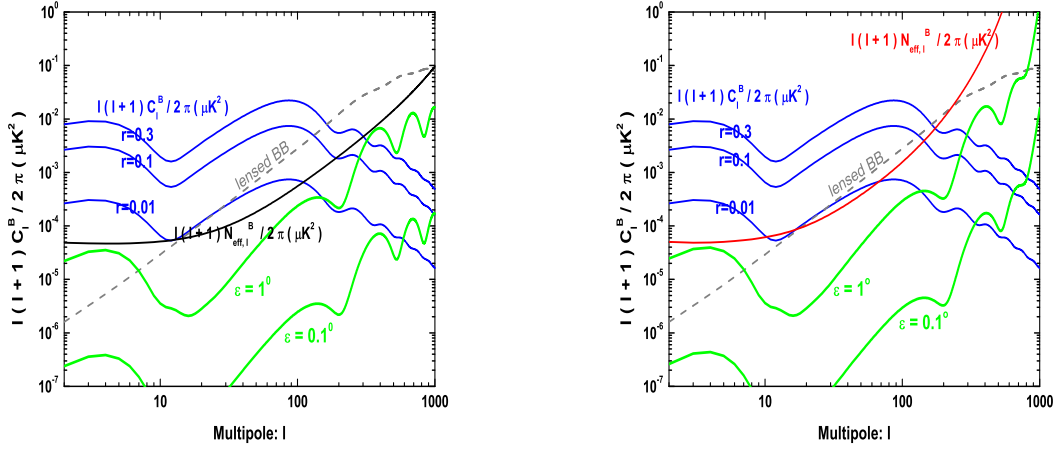


FIG. 18: The contribution of differential rotation to the B -polarization, comparing with the signal of C_ℓ^B for different r , the noise of CMBPol mission, and the lensed B -polarization. Left panel is for EPIC-2m, and the right panel is for EPIC-LC.

- [1] J. Bock *et al.*, *Task force on cosmic microwave background research*, [arXiv:astro-ph/0604101].
 [2] L. P. Grishchuk, Zh. Eksp. Teor. Fiz. *Amplification of gravitational waves in an isotropic universe*, **67**, 825 (1974) [Sov. Phys. JETP **40**, 409 (1975)]; *Graviton creation in the early Universe*, Ann. NY Acad. Sci. **302**, 439 (1977); *Primordial*

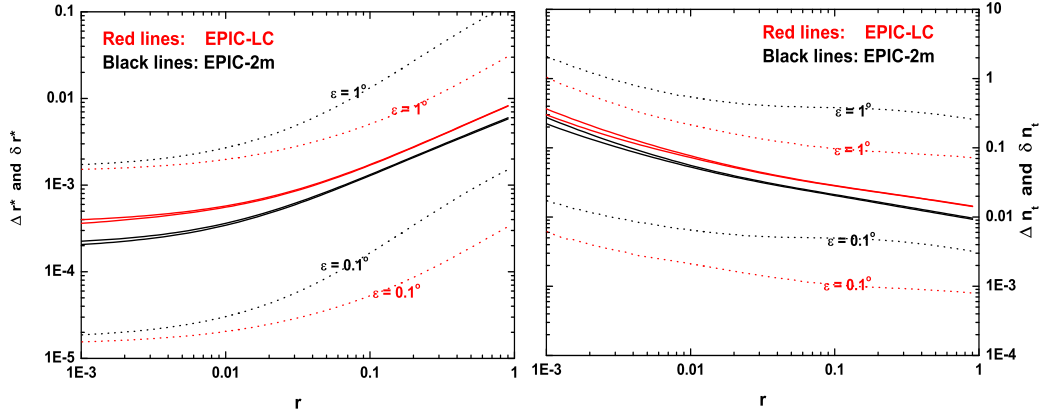


FIG. 19: The values of δr (left panel) and δn_t (right panel) from the differential rotation for different tensor-to-scalar ratio r . For the comparison, we plot the corresponding Δr and Δn_t in solid lines in the panels.

TABLE IV: Systematics tolerance for EPIC-2m and EPIC-LC, where different nominal values of r are considered. In each box, the left value is for the parameter r and the right value is for the parameter n_t .

	Nominal value	$\frac{g_c}{1\%} \sqrt{\frac{f_1}{2\pi}}$	$\frac{\mu_c}{1\%} \sqrt{\frac{f_1}{2\pi}}$	$\frac{\rho_c}{17} \sqrt{\frac{f_2}{2\pi}}$	$\frac{e_c}{1\%}$	ϵ_c [deg]
EPIC-2m	$r=0.001$	0.0017 & —	0.061 & 0.042	0.096 & 0.085	0.87 & 0.59	0.11 & 0.21
	$r=0.01$	0.0021 & —	0.049 & 0.030	0.087 & 0.071	0.70 & 0.43	0.11 & 0.14
	$r=0.1$	0.0031 & —	0.029 & 0.019	0.068 & 0.054	0.41 & 0.27	0.09 & 0.10
EPIC-LC	$r=0.001$	0.0020 & —	0.0073 & 0.0061	0.15 & 0.14	0.10 & 0.09	0.15 & 0.22
	$r=0.01$	0.0026 & —	0.0064 & 0.0053	0.14 & 0.13	0.09 & 0.08	0.17 & 0.19
	$r=0.1$	0.0039 & —	0.0050 & 0.0040	0.13 & 0.11	0.07 & 0.06	0.18 & 0.16

- gravitons and possibility of their observation*, Pis'ma Zh. Eksp. Teor. Fiz. **23**, 326 (1976) [JETP Lett. **23**, 293 (1976)].
- [3] L. P. Grishchuk, *Discovering relic gravitational waves in cosmic microwave background radiation*, Chapter in the "General Relativity and Johh Archibald Wheeler", edited by I. Ciufolini and R. Matzner, (Springer, New York, 2010, pp. 151-199), arXiv:0707.3319.
- [4] A. A. Starobinsky, *Spectrum of relict gravitational radiation and the early state of the Universe*, JETP Lett. **30**, 682 (1979).
- [5] V. A. Rubakov, M. Sazhin and A. Veryaskin, *Graviton creation in the inflationary universe and the grand unification scale*, Phys. Lett. B **115**, 189 (1982).
- [6] S. Sasaki, *Large scale quantum fluctuations in the inflationary universe*, Prog. Theor. Phys. **76**, 1036 (1986).
- [7] V. F. Mukhanov, H. A. Feldman and R. H. Brandenberger, *Theory of cosmological perturbations*, Phys. Rep. **215**, 203 (1992).
- [8] L. P. Grishchuk, *Relic gravitational waves and their detection*, Lect. Notes Phys. **562**, 167 (2001);
Y. Zhang, Y. F. Yuan, W. Zhao and Y. T. Chen, *Relic gravitational waves in the accelerating Universe*, Class. Quant. Grav. **22**, 1383 (2005);
T. L. Smith, H. V. Peiris and A. Cooray, *Deciphering inflation with gravitational waves: Cosmic microwave background polarization vs direct detection with laser interferometers*, Phys. Rev. D **73**, 123503 (2006);
W. Zhao and Y. Zhang, *Relic gravitational waves and their detection*, Phys. Rev. D **74**, 043503 (2006).
- [9] Y. Watanabe and E. Komatsu, *Improved calculation of the primordial gravitational wave spectrum in the standard model*, Phys. Rev. D **73**, 123515 (2006);
L. A. Boyle and P. J. Steinhardt, *Probing the early universe with inflationary gravitational waves*, Phys. Rev. D **77**, 063504 (2008);
M. Giovannini, *Production and detection of relic gravitons in quintessential inflationary models*, Phys. Rev. D **60**, 123511

- (1999), *Spikes in the relic graviton background from quintessential inflation*, *Class. Quant. Grav.* **16**, 2905 (1999), *Stochastic backgrounds of relic gravitons, Λ CDM paradigm and the stiff ages*, *Phys. Lett. B* **668**, 44 (2008), *Thermal history of the plasma and high-frequency gravitons*, *Class. Quant. Grav.* **26**, 045004 (2009).
- [10] D. H. Lyth and A. Riotto, *Particle physics models of inflation and the cosmological density perturbation*, *Phys. Rep.* **314**, 1 (1999).
- [11] S. Kachru *et al.*, *Towards inflation in string theory*, *JCAP*, **0310**, 013 (2003);
D. Baumann and L. McAllister, *A microscopic limit on gravitational waves from D-brane inflation*, *Phys. Rev. D* **75**, 123508 (2007);
E. Silverstein and D. Tong, *Scalar speed limits and cosmology: Acceleration from D-acceleration*, *Phys. Rev. D* **70**, 103505 (2004);
R. Kallosh and A. Liddle, *Testing string theory with CMB*, *JCAP*, **0704**, 017 (2007).
- [12] A. Polnarev, *Polarization and anisotropy induced in the microwave background by cosmological gravitational waves*, *Sov. Astron.* **29**, 607 (1985);
D. Harari and M. Zaldarriaga, *Polarization of the microwave background in inflationary cosmology*, *Phys. Lett. B* **319**, 96 (1993);
L. P. Grishchuk, *Cosmological perturbations of quantum-mechanical origin and anisotropy of the microwave background*, *Phys. Rev. Lett.* **70**, 2371 (1993);
R. Crittenden, J. R. Bond, R. L. Davis, G. Efstathiou and P. J. Steinhardt, *Imprint of gravitational waves on the cosmic microwave background*, *Phys. Rev. Lett.* **71**, 324 (1993);
R. A. Frewin, A. G. Polnarev and P. Coles, *Gravitational waves and the polarization of the cosmic microwave background*, *Mon. Not. R. Astron. Soc.* **266**, L21 (1994).
- [13] U. Seljak and M. Zaldarriaga, *Signature of gravity waves in the polarization of the microwave background*, *Phys. Rev. Lett.* **78**, 2054 (1997);
M. Kamionkowski, A. Kosowsky and A. Stebbins, *A probe of primordial gravity waves and vorticity*, *Phys. Rev. Lett.* **78**, 2058 (1997).
- [14] M. Zaldarriaga and U. Seljak, *All-sky analysis of polarization in the microwave background*, *Phys. Rev. D* **55**, 1830 (1997).
- [15] J. R. Pritchard and M. Kamionkowski, *Cosmic microwave background fluctuations from gravitational waves: An analytic approach*, *Ann. Phys. (N.Y.)* **318**, 2 (2005);
W. Zhao and Y. Zhang, *Analytic approach to the CMB polarization generated by relic gravitational waves*, *Phys. Rev. D* **74**, 083006 (2006);
D. Baskaran, L. P. Grishchuk and A. G. Polnarev, *Imprints of relic gravitational waves in cosmic microwave background radiation*, *Phys. Rev. D* **74**, 083008 (2006);
T. Y. Xia and Y. Zhang, *Analytic spectra of CMB anisotropies and polarization generated by relic gravitational waves with modification due to neutrino free-streaming*, *Phys. Rev. D* **78**, 123005 (2008), *Approximate analytic spectra of reionized CMB anisotropies and polarization generated by relic gravitational waves*, *Phys. Rev. D* **79**, 083002 (2009).
- [16] B. G. Keating, A. G. Polnarev, N. J. Miller and D. Baskaran, *The polarization of the cosmic microwave background due to primordial gravitational waves*, *Int. J. Mod. Phys. A* **21**, 2459 (2006);
R. Flauger and S. Weinberg, *Tensor microwave background fluctuations for large multipole order*, *Phys. Rev. D* **75**, 123505 (2007);
Y. Zhang, W. Zhao, X. Z. Er, H. X. Miao and T. Y. Xia, *Relic gravitational waves and CMB polarization in the accelerating Universe*, *Int. J. Mod. Phys. D* **17**, 1105 (2008).
- [17] A. G. Polnarev, N. J. Miller and B. G. Keating, *CMB temperature polarization correlation and primordial gravitational waves*, *Mon. Not. R. Astron. Soc.* **386**, 1053 (2008);
N. J. Miller and B. G. Keating and A. G. Polnarev, *CMB temperature polarization correlation and primordial gravitational waves II: Wiener filtering and tests based on Monte Carlo simulations*, arXiv:0710.3651.
- [18] W. Zhao, D. Baskaran and L. P. Grishchuk, *On the road to discovery of relic gravitational waves: The TE and BB correlations in the cosmic microwave background radiation*, *Phys. Rev. D* **79**, 023002 (2009).
- [19] E. Komastu *et al.*, *Seven-Year Wilkinson Microwave Anisotropy Probe (WMAP) observations: Cosmological interpretation*, arXiv:1001.4538.
- [20] W. Zhao, D. Baskaran and L. P. Grishchuk, *On the road to discovery of relic gravitational waves: The TE and BB correlations in the cosmic microwave background radiation*, *Phys. Rev. D* **79**, 023002 (2009), *Stable indications of relic gravitational waves in Wilkinson Microwave Anisotropy Probe data and forecasts for the Planck mission*, *Phys. Rev. D* **80**, 083005 (2009), *Relic gravitational waves in light of the 7-year Wilkinson Microwave Anisotropy Probe data and improved prospects for the Planck mission*, *Phys. Rev. D* **82**, 043003 (2010);
W. Zhao and L. P. Grishchuk, *Relic gravitational waves: Latest revisions and preparations for new data*, *Phys. Rev. D* **82**, 123008 (2010).
- [21] Planck Collaboration, *The science programme of Planck*, [arXiv:astro-ph/0604069].
- [22] W. Zhao, *Detecting relic gravitational waves in the CMB: Comparison of different methods*, *Phys. Rev. D* **79**, 063003 (2009).
- [23] Y. Z. Ma, W. Zhao and M. L. Brown, *Constraints on standard and non-standard early Universe models from CMB B-mode polarization*, *JCAP*, **1010**, 007 (2010).
- [24] W. Zhao and D. Baskaran, *Detecting relic gravitational waves in the CMB: Optimal parameters and their constraints*, *Phys. Rev. D* **79**, 083003 (2009).
- [25] B. G. Keating *et al.*, *BICEP: A large angular scale CMB polarimeter*, in *Polarimetry in Astronomy*, edited by Silvano

- Fineschi, Proceedings of the SPIE, **4843** (2003);
 C. Pryke *et al.*, QUaD Collaboration, *Second and third season QUaD CMB temperature and polarization power spectra*, Astrophys. J. **692**, 1247 (2009);
 A. C. Taylor, Clover Collaboration, *Clover - A B-mode polarization experiment*, New Astron. Rev. **50**, 993 (2006);
 J. Errard, *The new generation CMB B-mode polarization experiment: POLARBEAR*, arXiv:1011.0763;
<http://bolo.berkeley.edu/polarbear/index.html>;
 D. Samtleben, *Measuring the cosmic microwave background radiation (CMBR) polarization with QUIET*, arXiv:0802.2657;
<http://quiet.uchicago.edu/>;
 J.A. Rubino-Martin *et al.*, *The Quijote CMB Experiment*, arXiv:0810.3141;
<http://www.iac.es/project/cmb/quijote/>;
<http://pole.uchicago.edu/>;
<http://www.phy.princeton.edu/act/>;
 The QUBIC Collaboration, *QUBIC: The QU Bolometric Interferometer for Cosmology*, arXiv:1010.0645.
- [26] <http://groups.physics.umn.edu/cosmology/ebex/index.html>;
 A. Kogut, *et al.*, *PAPPA: Primordial Anisotropy Polarization Pathfinder Array*, New Astron. Rev. **50**, 1009 (2006);
 B.P. Crill, *et al.*, *SPIDER: A balloon-borne large-scale CMB polarimeter*, arXiv:0807.1548.
- [27] W. Zhao and W. Zhang, *Detecting relic gravitational waves in the CMB: Comparison of Planck and ground-based experiments*, Phys. Lett. B **677**, 16 (2009).
- [28] D. Baumann *et al.*, *CMBPol mission concept study: Probing inflation with CMB polarization*, arXiv:0811.3919.
- [29] B-Pol Collaboration, *B-Pol: Detecting primordial gravitational waves generated during inflation*, Exper. Astron. **23**, 5 (2009);
<http://www.b-pol.org/index.php>.
- [30] <http://cmbpol.kek.jp/litebird/>.
- [31] L. P. Grishchuk and M. Solokhin, *Spectra of relic gravitons and the early history of the Hubble parameter*, Phys. Rev. D **43**, 2566 (1991);
 A. Kosowsky and M. S. Turner, *CMB anisotropy and the running of the scalar spectral index*, Phys. Rev. D **52**, 1739 (1995).
- [32] E. D. Stewart and D. H. Lyth, *A more accurate analytic calculation of the spectrum of cosmological perturbations produced during inflation*, Phys. Lett. B **302**, 171 (1993).
- [33] H. V. Peiris *et al.*, *First Year Wilkinson Microwave Anisotropy Probe (WMAP) observations: Implications for inflation*, Astrophys. J. Suppl. Ser. **148**, 213 (2003).
- [34] E. Komatsu *et al.*, *Five-Year Wilkinson Microwave Anisotropy Probe (WMAP) observations: Cosmological interpretation*, Astrophys. J. Suppl. Ser. **180**, 330 (2009).
- [35] A. Lewis, A. Challinor and A. Lasenby, *Efficient computation of CMB anisotropies in closed FRW models*, Astrophys. J. **538**, 473 (2000);
<http://camb.info/>.
- [36] M. J. Mortonson and W. Hu, *Model-independent constraints on reionization from large-scale CMB polarization*, Astrophys. J. **672**, 737 (2008);
 M. J. Mortonson and W. Hu, *Impact of reionization on CMB polarization tests of slow-roll inflation*, Phys. Rev. D **77**, 043506 (2008);
 M. J. Mortonson and W. Hu, *Reionization constraints from five-year WMAP data*, Astrophys. J. **686**, L53 (2008).
- [37] S. Hamimeche and A. Lewis, *Likelihood analysis of CMB temperature and polarization power spectra*, Phys. Rev. D **77**, 103013 (2008).
- [38] W. J. Percival and M. L. Brown, *Likelihood methods for the combined analysis of CMB temperature and polarisation power spectra*, Mon. Not. R. Astron. Soc. **372**, 1104 (2006);
 H. K. Eriksen and I. K. Wehus, *Marginal distributions for cosmic variance limited CMB polarization data*, Astrophys. J. Suppl. Ser. **180**, 30 (2009).
- [39] A. Lewis and S. L. Bridle, *Cosmological parameters from CMB and other data: A Monte Carlo approach*, Phys. Rev. D **66**, 103511 (2002).
- [40] A. Lewis, *Harmonic E/B decomposition for CMB polarization maps*, Phys. Rev. D **68**, 083509 (2003);
 A. Lewis, A. Challinor and N. Turok, *Analysis of CMB polarization on an incomplete sky*, Phys. Rev. D **65**, 023505 (2001);
 E. F. Bunn, M. Zaldarriaga, M. Tegmark and A. de Oliveira-Costa, *E/B decomposition of finite pixelized CMB maps*, Phys. Rev. D **67**, 023501 (2003);
 E. F. Bunn, *E/B mode mixing*, arXiv:0811.0111; *Efficient decomposition of cosmic microwave background polarization maps into pure E, pure B, and ambiguous components*, arXiv:1008.0827.
- [41] K. M. Smith, *Pseudo-Cl estimators which do not mix E and B modes*, Phys. Rev. D **74**, 083002 (2006);
 J. Grain, M. Tristram and R. Stompor, *Polarized CMB power spectrum estimation using the pure pseudo-cross-spectrum approach*, Phys. Rev. D **79**, 123515 (2009);
 K. M. Smith and M. Zaldarriaga, *General solution to the E-B mixing problem*, Phys. Rev. D **76**, 043001 (2007).
- [42] W. Zhao and D. Baskaran, *Separating E and B types of polarization on an incomplete sky*, Phys. Rev. D **82**, 023001 (2010);
 J. Kim and P. Naselsky, *CMB E/B decomposition of incomplete sky: a pixel space approach*, Astronomy and Astrophysics **519**, A104 (2010);
 J. Kim, *How to make clean separation of CMB E and B mode from incomplete sky data*, arXiv:1010.2636.
- [43] J. Bock *et al.*, *Study of the Experimental probe of Inflationary Cosmology (EPIC)-Intermediate mission for NASA's Einstein Inflation Probe*, arXiv:0906.1188.

- [44] M. Zaldarriaga and U. Seljak, *Gravitational lensing effect on cosmic microwave background polarization*, Phys. Rev. D **58**, 023003 (1998).
- [45] W. Hu and T. Okamoto, *Mass reconstruction with CMB polarization*, Astrophys. J. **574**, 566 (2002);
T. Okamoto and W. Hu, *CMB lensing reconstruction on the full sky*, Phys. Rev. D **67**, 083002 (2003).
- [46] C. M. Hirata and U. Seljak, *Reconstruction of lensing from the cosmic microwave background polarization*, Phys. Rev. D **68**, 083002 (2003);
U. Seljak and C. M. Hirata, *Gravitational lensing as a contaminant of the gravity wave signal in the CMB*, Phys. Rev. D **69**, 043005 (2004).
- [47] A. Lewis and A. Challinor, *Weak gravitational lensing of the CMB*, Phys. Rep. **429**, 1 (2006).
- [48] K. M. Smith *et al.*, *CMBPol mission concept study: Gravitational lensing*, arXiv:0811.3916.
- [49] L. Knox and Y. S. Song, *Limit on the detectability of the energy scale of inflation*, Phys. Rev. Lett. **89**, 011303 (2002);
M. Kesden, A. Cooray and M. Kamionkowski, *Separation of gravitational-wave and cosmic-shear contributions to cosmic microwave background polarization*, Phys. Rev. Lett. **89**, 011304 (2002).
- [50] C. L. Bennett *et al.*, *First Year Wilkinson Microwave Anisotropy Probe (WMAP) observations: Foreground emission*, Astrophys. J. Suppl. Ser. **148**, 97 (2003).
- [51] J. Dunkely *et al.*, *CMBPol mission concept study: Prospects for polarized foreground removal*, arXiv:0811.3915.
- [52] L. Verde, H. Peiris and R. Jimenez, *Considerations in optimizing CMB polarization experiments to constrain inflationary physics*, JCAP, **0601**, 019 (2006).
- [53] L. Page *et al.*, *Three Year Wilkinson Microwave Anisotropy Probe (WMAP) Observations: Polarization Analysis*, Astrophys. J. Suppl. Ser. **170**, 335 (2007).
- [54] E. M. Finkbeiner *et al.*, *Extrapolation of galactic dust emission at 100 microns to CMBR frequencies using FIRAS*, Astrophys. J. **624**, 10 (2001).
- [55] J. Kim, P. Naselsky and P. R. Christensen, *CMB polarization map derived from the WMAP 5 year data through the harmonic internal linear combination method*, Phys. Rev. D **79**, 023003 (2009);
G. Efstathiou, S. Gratton and F. Paci, *Impact of galactic polarized emission on B-mode detection at low multipoles*, Mon. Not. Roy. Astron. Soc. **397**, 1355 (2009).
- [56] W. Zhao and Q. G. Huang, *Testing inflationary consistency relations by the potential CMB observations*, arXiv:1101.3163.
- [57] W. Hu, M. M. Hedman and M. Zaldarriaga, *Benchmark parameters for CMB polarization experiments*, Phys. Rev. D **67**, 043004 (2003).
- [58] M. Su, A. P. S. Yadav and M. Zaldarriaga, *Impact of instrumental systematic contamination on the lensing mass reconstruction using the CMB polarization*, Phys. Rev. D **79**, 123002 (2009);
M. Su, A. P. S. Yadav, M. Shimon and B. G. Keating, *Impact of instrumental systematics on the CMB bispectrum*, arXiv:1010.1957.
- [59] M. Shimon, B. Keating, N. Ponthieu and E. Hivon, *CMB polarization systematics due to beam asymmetry: Impact on inflationary science*, Phys. Rev. D **77**, 083003 (2008);
N. J. Miller, M. Shimon and B. G. Keating, *CMB beam systematics: Impact on lensing parameter estimation*, Phys. Rev. D **79**, 063008 (2009); *CMB polarization systematics due to beam asymmetry: Impact on cosmological birefringence*, Phys. Rev. D **79**, 103002 (2009).
- [60] D. O’Dea, A. Challinor and B. R. Johnson, *Systematic errors in cosmic microwave background polarization measurements*, Mon. Not. Roy. Astron. Soc. **376**, 1767 (2007).
- [61] Note that in the real analysis throughout this paper, similar to [28], we have not considered the frequency channels at 30GHz and 340GHz proposed in [28] for EPIC-2m, and the frequency channels at 30GHz and 300GHz for EPIC-LC.
- [62] Note that, in Sec. V, we will show that the total noise level will be increased if the reduced foreground contaminations are considered. However, the noise level with high multipole $\ell > 100$ nearly keeps same.